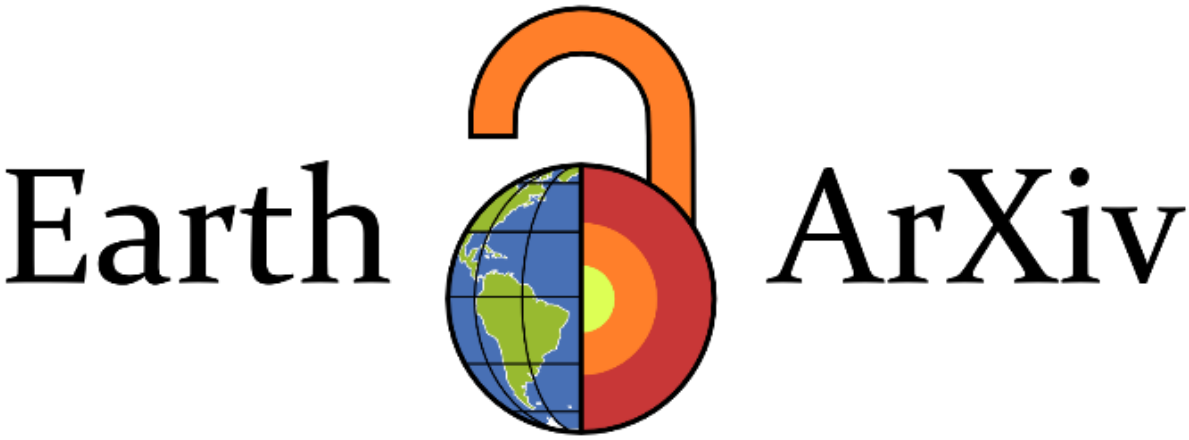

Crushability of Glauconite with Silica Sand

Shijin Li[1], Hannes Claes[2], Hadrien Rattez[3]

Shijin Li, PhD, [1] Institute of Mechanics, Materials and Civil Engineering, Université Catholique de Louvain, Louvain-la-Neuve, B-1348, Belgium. shijin.li@uclouvain.be. https://orcid.org/0000-0002-2918-3934

Hannes Claes, [2] Department of Earth and Environmental Sciences, Geology, KU Leuven, 3001 Leuven, Belgium. hannes.claes1@kuleuven.be. https://orcid.org/0000-0002-2424-6975.

Hadrien Rattez, [3] Institute of Mechanics, Materials and Civil Engineering, Université Catholique de Louvain, Louvain-la-Neuve, B-1348, Belgium. hadrien.rattez@uclouvain.be. https://orcid.org/0000-0002-7245-6563.

* (Corresponding author) Email: hadrien.rattez@uclouvain.be

Figures: xx (please refer to figure files for higher quality versions)

Tables: x

Main text word count: xxxx

ABSTRACT

Glauconite-rich sands are increasingly encountered in offshore and nearshore developments, yet their mechanical behaviour remains poorly understood owing to the extreme crushability of glauconite grains. Particle crushing in these sediments alters stiffness, compressibility, grading, particle morphology and, consequently, engineering performance. This study presents a comprehensive experimental programme to quantify the crushability of pure glauconite, glauconite-silica mixtures, and silica sand under one-dimensional compression. Loading-unloading oedometer tests arrested at different axial strains were conducted on five materials containing varying glauconite, in both dry and saturated conditions. High-resolution laser diffraction and dynamic image analysis were used to characterise the evolutions of particle size and shape. The results show that glauconite exhibits substantially lower yield stress and requires far less work input to initiate crushing than silica sand. Yielding stress and threshold work decrease nonlinearly with increasing glauconite content, while relative breakage grows approximately linearly with strain. All materials evolve toward finer, fractal particle size distributions, and a robust exponential relationship between relative breakage and fractal dimension is established. Shape analysis reveals progressive elongation and edge irregularity with breakage, with glauconite retaining more equant geometries compared with silica. By integrating stress-strain behaviour, energy dissipation, grading evolution, and particle-shape change, this work presents a unified experimental framework for understanding crushing of glauconitic sands. The results support improved offshore foundation design, breakage-aware constitutive modelling, and assessments of pile installation and long-term performance in glauconite-rich deposits.

Keywords: Glauconite; oedometer test; crushing; particle size distribution; particle shape evolution

1. Introduction

Glauconite is a green, iron-potassium phyllosilicate mineral that forms predominantly in shallow marine environments, typically appearing as small rounded pellets that impart the characteristic green colour of "greensands" (Tedrow, 2002). Because of their weak, brittle, and micro-porous internal structure, glauconite grains crush readily under relatively low stresses, causing the material to rapidly transform from a stiff, permeable coarse-grained sand into a weak, low-permeability fine-grained soil. Glauconite-rich sands are increasingly encountered in nearshore and offshore geotechnical projects, particularly along shallow marine shelves where wind farm development is rapidly expanding (De Nijs et al., 2015; Westgate et al., 2022). Their widespread geological occurrence, combined with their highly crushable nature, poses substantial challenges for foundation design and soil-structure interaction analyses (De Nijs et al., 2015; Baldermann et al., 2022; Westgate et al., 2022, 2023, 2024). For offshore wind farm developments, for example, monopile foundations, these breakage-induced changes can be critical, as loading paths commonly involve high stress concentrations and high number of cyclic stress reversals. Nearshore, glauconitic soils similarly compromise the performance of embankments, ground improvement works, and pile installations due to their tendency to undergo excessive grading evolution under compaction or driving.

Although glauconite occurs widely in shallow marine deposits, its permissible content in engineering applications remains a critical concern (Westgate et al., 2022). Van Raak (2009) classified glauconite sands as low (<5%), medium (5-40%) and high (>40%) in content, and Belgian guidelines (Tedrow, 2002) further restrict glauconite to <5% for construction sand, allowing its use primarily in embankments. Yet laboratory and field observations are inconsistent. For example, Thanet Sand with up to 10% glauconite exhibited benign behaviour during the London Crossrail project (Ventouras and Coop, 2009), and later investigations reported little adverse impact at

similar contents (Mentiki et al., 2015). Conversely, direct shear tests on glauconitic sands (Van Raak, 2009) showed marked differences in stress-strain response across 100% glauconite, 54% glauconite and pre-crushed 100% glauconite (the latter having up to 6% additional fines due to pre-crushing), exhibiting a clear transition from strain-softening to strain-hardening behaviour, despite their critical-state friction angles differing by only about 2°. A similar transition has also been reported by Konstantinou et al. (2025). North Sea monopile driving data also indicate that even modest glauconite contents (~5 to 20%) can substantially increase the pile-sand interface shear resistance (Perikleous et al., 2023). These mixed observations suggest that glauconite content influences soil behaviour in complex and non-intuitive ways, and that current empirical guidelines do not fully capture this variability.

Existing studies consistently show that glauconite sands exhibit a high propensity for particle breakage, with crushability strongly influenced by glauconite content and particle angularity. Laboratory observations, including triaxial compression tests (Hossain et al., 2009), oedometer tests (Emidio et al., 2009) and direct shear tests (Westgate et al., 2023; Zou et al., 2025), report glauconite undergoes substantial crushing, often extensively than calcareous or carbonate sands, and that this process is accompanied by marked changes in particle roundness. Notably, glauconite particles may crush at relatively low stress levels, with crushing reported to initiate at stresses as low as 2 MPa in oedometer tests (Bellotti et al., 1991). The engineering implications of this crushability are significant. Breakage-generated fines modify soil plasticity, shear strength, and thixotropy, and have been linked to early pile refusal, increased shaft friction, and reductions in pile capacity with depth (Van Raak, 2009; Westgate et al., 2024). Field observations in Belgium and the North Sea further demonstrate that pile driving can induce substantial grain breakage along the pile wall, altering soil setup and long-term capacity, particularly when vibratory or hammer installation methods are used (De Nijs et al., 2015). Despite these insights, current

understanding still lacks quantitative, mineral-specific evidence linking glauconite content to particle breakage mechanisms, grading evolution, and resultant macro-mechanical behaviour. Addressing this knowledge gap requires systematic laboratory investigations capable of isolating glauconite content as a controlling variable.

Recent advances in particle-crushing research have greatly improved the ability to quantify particle size and shape evolution. Arrested-loading tests and high-resolution imaging techniques now allow particle size and shape evolutions to be quantified (Suescun-Florez et al., 2020). Complementary studies on carbonate and silica sands have clarified how stress level, relative density, strain rate and coordination number control breakage, while energy-based frameworks link macroscopic input work to particle-scale fracture mechanisms (Zhang et al., 2016; Huang et al., 2017; Xiao et al., 2017, 2019; Zhao et al., 2020; Wu et al., 2020; Lei et al., 2024). More recent theoretical developments further highlight the need to incorporate coevolving grain size and shape descriptors into constitutive models, recognising that particle morphology evolves during comminution and directly influences macroscopic behaviour (Buscarnera and Einav, 2021). Together, these advances provide a strong foundation for interpreting breakage mechanics, grading evolution, and shape modification in brittle granular materials. However, these experimental and theoretical tools have not yet been systematically applied to glauconite sands, whose crushability, grading evolution, and energy-breakage relationships remain insufficiently understood despite their pronounced susceptibility to fragmentation and growing relevance in offshore and nearshore geotechnics.

Motivated by these gaps, a comprehensive experimental programme was undertaken to quantify the crushability of sands containing varying glauconite contents and to determine how glauconite content governs particle size and shape evolutions and macroscopic stress strain response and compressibility. The objectives were to: (1)

characterise the mechanical response and yielding behaviour of pure glauconite, glauconite-silica mixtures, and silica sand under one-dimensional compression, and (2) develop quantitative relationships linking stress, energy dissipation, relative breakage, fractal grading evolution, and particle-shape change. Arrested loading-unloading oedometer tests were performed on five materials, complemented by high-resolution particle size and shape measurements. The resulting dataset provides new insight into the mineral-dependent fragmentation behaviour of glauconite and establishes an experimental framework that links particle-scale breakage to macro-scale compressibility and energy dissipation. These findings enhance the understanding of crushing in glauconitic deposits and support improved offshore foundation design, constitutive modelling, and assessments of pile installation and long-term performance in glauconite-rich sands.

2. Testing materials and methods

2.1. Testing materials

1. Geological and geotechnical properties
2. A schematic diagram of glauconite formation in Belgium
3. Sampling and sample preparation

Difference in level of maturity, O

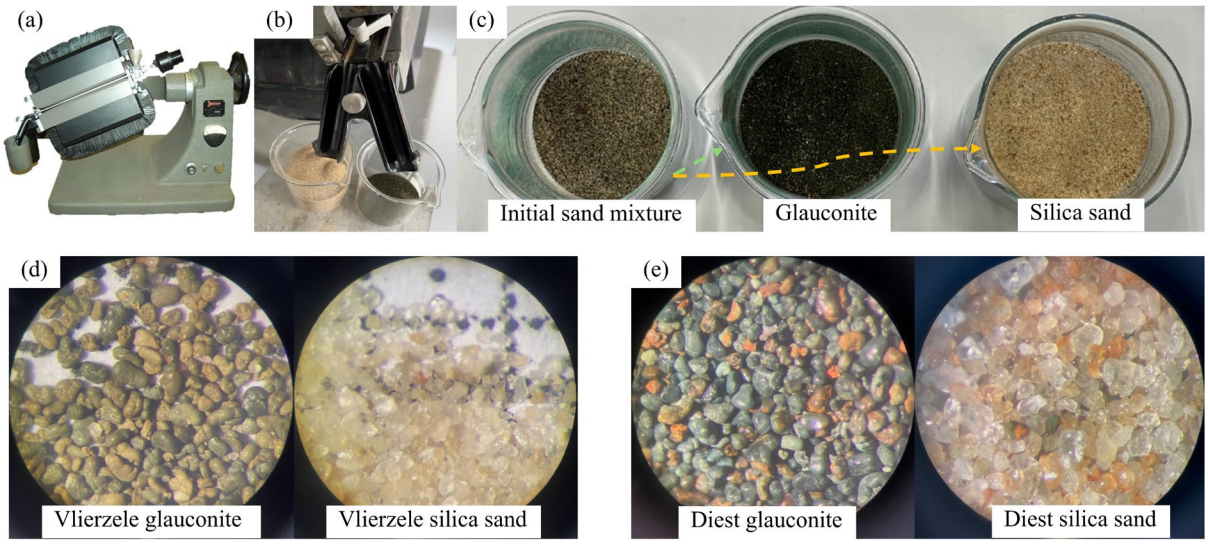

123

124 **Fig.** 1. (a) Frantz magnetic separator; (b) Separated sands; (c) initial sand mixture alongside separated glauconite
125 and silica sand; (d) photographs of 100% Vlierzele glauconite and silica sand; (e) photos of 100% Diest glauconite
126 and silica sand (Red-coloured particle surfaces indicate oxidation).

127 D50,

128 Magnetically separate glauconite from silica sand (Westgate et al., 2023).

129

130 ***2.2. Testing apparatus and testing procedures***

131 2.2.1 Oedometer cell

132 A stainless steel oedometer cell was designed to systematically investigate the stress-strain behaviour of glauconite
133 and silica sand mixtures under high pressure. The oedometer cell is consist of a top force transmission cap with
134 19.5 mm diameter loading rod, a thick-walled cylinderical cell, a base with a drainage channel and stainless
135 top/bottom discs for dry tests and porous copper discs for saturated tests (19.8 mm diameter), as illustrated in in
136 Fig. 3 (a) and Fig. 3 (b). The cylindrical cell was designed with an outer diameter of 60 mm, an inner diameter of
137 20 mm, and a wall thickness of 40 mm, ensuring that the radial deformation under 400 MPa remain negligible
138 (i.e., $< 1\%$, given the Young's modulus of 200 GPa and the Poisson's ratio of 0.26).

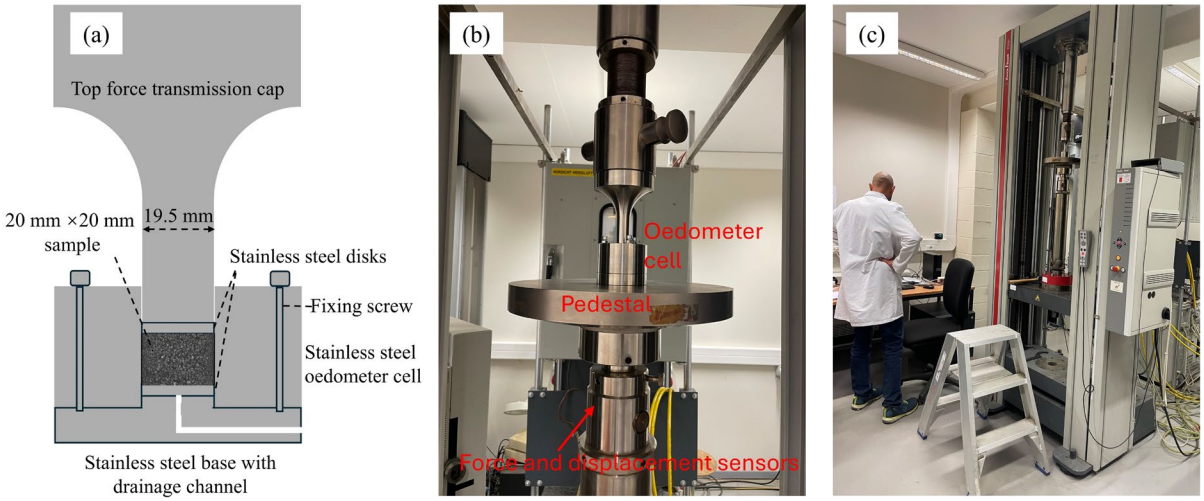

Fig. 2. (a) schematic drawing of the oedometer cell; (b) photograph of the oedometer cell positioned in the loading system; (c) a photo of the overview of the loading system

2.2.2 Loading system

A Zwick Roell Z250 materials testing machine (as shown in Fig. 3 (C)), equipped with a central ball-lead screw, was used to apply and maintain loading and unloading forces on the samples placed in the oedometer cell. The axial displacement was controlled via programmable software, with both force and displacement automatically recorded throughout each test. The machine has a maximum compression force of 250 kN, corresponds to a maximum compressive stress of approximately 2,500 MPa for a sample with a 20 mm diameter.

2.2.3 Particle size and shape quantification system

Conventional sieve analysis was unsuitable for the present study because the particle sizes of the tested materials were too fine to be accurately classified, while hydrometer testing proved inefficient for resolving the complete particle size distribution (PSD). Dynamic imaging techniques, although capable of measuring fine particles, are sensitive to particle orientation during measurement since three-dimensional bodies must be represented by two-

or one-dimensional parameters (Altuhafi et al., 2013; Suescun-Florez et al., 2020). In recent years, laser diffraction has become a widely adopted technique for estimating PSDs (Eshel et al., 2004). However, this method encounters limitations when applied to irregularly shaped particles, where defining an equivalent spherical diameter is challenging. To overcome these limitations, integrated systems combining laser diffraction with high-speed dynamic imaging have been developed and are now extensively used in soil characterization, enabling simultaneous and reliable analysis of both particle size and shape. In this study, the Microtrac SYNC particle size and shape analyzer, which integrates laser diffraction with dynamic image analysis within a single instrument, was emplyed to quantitatively determine particle size distributions and morphological parameters. This hybrid technique enables simultaneous measurement of particle size and shape characteristics under identical testing conditions (Grubbs et al., 2021). The system measures particles ranging from 0.3 μm to 2000 μm. A schematic diagram and a photograph of the analyzer are shown in Fig. 4.

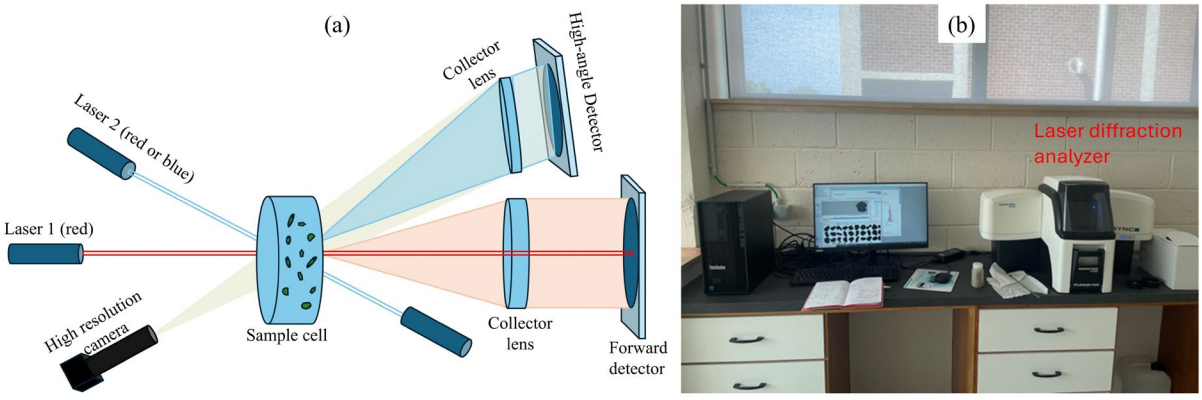

Fig. 3. (a) Schematic diagram of the laser diffraction analyzer with a tri-laser system integrated with dynamic imaging; (b) photograph of the Microtrac SYNC particle size and shape analyzer.

2.3. Testing procedures

2.3.1 Oedometer tests

The arrested loading-unloading technique described by Suescun-Florez et al. (2020) was adopted in this study. This method involves unloading the specimen after reaching a predetermined strain level to determine the unloading modulus and to enable post-test determination of the material's particle size distribution and morphological parameters.

Prior to sample preparation, the shaft of the top disk, the inner wall of the cylindrical cell and the loading rod were lubricated with a thin layer of silicone grease to minimize friction. A calculated mass of dry material was carefully poured into the oedometer cell using a funnel with a long shaft (approximately 5 cm). The sample was then subjected to vibration for 1-3 minutes to achieve the target height, ensuring a uniform density and void ratio (Suescun-Florez et al., 2020). Stainless steel top and bottom discs for dry tests, and porous copper discs for saturated tests, as illustrated in Fig. 3 (a), were placed on the bottom and top surfaces of the specimen..

Before each loading-unloading cycle, a preload force was applied until it reached 10 N (≈31.8 kPa) to ensure full contact between the components and the sample. Loading commenced immediately once the preload force was achieved. A constant displacement rate of 0.1 mm/min was applied during loading and 1 mm/min during unloading.

For tests on dry samples, strain-controlled compression tests were conducted under continuous loading (CL). Each series of tests on the same material was arrested at axial strains ranging from 10% to 40%. For silica sand, the maximum strain was limited to 30% to avoid excessive loading stress that could cause deformation or yielding of

192 the steel loading rod. Once the target strain was achieved, the load was held constant for 1 s, after which unloading
193 commenced.
194
195 For tests on saturated samples, after sample preparation, water was added to a level approximately 1 cm above
196 the specimen surface, and the saturation process was maintained for 12 hours before loading. An incremental
197 loading (IL) technique, following ASTM D2435 (2020), was then employed. Specifically, the sample was loaded
198 in multiple increments, with each load step corresponding to a predetermined strain level equivalent to
199 approximately 1 mm of axial displacement. After each increment, the load was maintained for fixed durations of
200 1, 2, 4, 4, 4, and 4 hours, respectively, to allow pore water pressure dissipation and ensure that primary
201 consolidation was substantially completed before proceeding to the next increment. This stepwise loading process
202 continued until the final target strain was reached, after which the sample was unloaded. For comparison,
203 additional tests using the constant loading (CL) technique were conducted on the same material.
204
205 In this study, five materials were tested: 100% Diest Glauconite, 100% Vlierzele Glauconite, 32.4% Diest
206 Glauconite mixed with silica sand, 7.8% Vlierzele Glauconite mixed with silica sand, and pure silica sand. The
207 latter was used as a benchmark for comparing glauconitic sands with typical sand behaviour. A summary of the
208 oedometer tests, including sample type, testing condition, loading mode, and corresponding strain and stress
209 parameters, is presented in Table 1.
210
211 **Table 1** Summary of oedometer tests in this study

Test NO.	Test sample (Glauconite content)	Sampling location	Condition	ε_{target}	ε_{max}	Loading rate (mode) (mm/min)	e_0	σ_y (MPa)	σ_{max} (MPa)

1	100% Glauconite	Diest	Dry	10%	11.2%	0.1 (CL)	0.877	5.16	9.83
2	100% Glauconite	Diest	Dry	15%	15%	0.1 (CL)	0.877	5.16	12.13
3	100% Glauconite	Diest	Dry	20%	21.8%	0.1 (CL)	0.895	5.16	24.98
4	100% Glauconite	Diest	Dry	30%	30.4%	0.1 (CL)	0.886	5.16	42.01
5	100% Glauconite	Diest	Dry	40%	40%	0.1 (CL)	0.888	5.16	94.42
6	100% Glauconite	Diest	Saturated	30%	29.8%	0.1 (CL)	0.879	0.45	6.14
7	100% Glauconite	Diest	Saturated	50%	49.4%	0.1 (CL)	0.885	0.45	74.23
8	100% Glauconite	Diest	Saturated	30%	35%	0.1 (IL)	0.877	0.47	7.37
9	100% Glauconite	Diest	Saturated	30%	36%	0.1 (IL)	0.826	0.47	4.57
10	100% Glauconite	Vlierzele	Dry	10%	10.2%	0.1 (CL)	0.902	5.76	9.03
11	100% Glauconite	Vlierzele	Dry	20%	20.3%	0.1 (CL)	0.909	5.76	21.11
12	100% Glauconite	Vlierzele	Dry	30%	30.6%	0.1 (CL)	0.907	5.76	42.33
13	100% Glauconite	Vlierzele	Dry	40%	40.4%	0.1 (CL)	0.911	5.76	84.22
14	32.4% Glauconite	Diest	Dry	10%	10.0%	0.1 (CL)	0.876	6.62	15.92
15	32.4% Glauconite	Diest	Dry	20%	19.7%	0.1 (CL)	0.887	6.62	35.16
16	32.4% Glauconite	Diest	Dry	30%	29.4%	0.1 (CL)	0.874	6.62	81.72
17	32.4% Glauconite	Diest	Dry	40%	39.8%	0.1 (CL)	0.888	6.62	222.93
18	7.8% Glauconite	Vlierzele	Dry	10%	9.9%	0.1 (CL)	0.903	10.78	21.44
19	7.8% Glauconite	Vlierzele	Dry	20%	19.6%	0.1 (CL)	0.896	10.78	47.58
20	7.8% Glauconite	Vlierzele	Dry	30%	29.3%	0.1 (CL)	0.897	10.78	106.04
21	7.8% Glauconite	Vlierzele	Dry	40%	36.3%	0.1 (CL)	0.897	10.78	222.94
22	7.8% Glauconite	Vlierzele	Dry	40%	38.3%	0.1 (CL)	0.901	10.78	260.58
23	100% silica sand	Diest	Dry	10%	10.1%	0.1 (CL)	0.863	14.95	27.27
24	100% silica sand	Diest	Dry	20%	20.0%	0.1 (CL)	0.880	14.95	61.98
25	100% silica sand	Diest	Dry	30%	30.02%	0.1 (CL)	0.867	14.95	165.49
26	100% silica sand	Diest	Saturated	30%	35.3%	0.1 (IL)	0.863	14.85	157.66

Note: ε_{max} denotes the maximum axial strain; CL denotes continuous loading with a constant loading rate; IL denotes incremental loading

2.3.2 Particle size and shape analysis

After each arrested test, the entire material was collected and prepared for subsequent particle size and shape analyses. Glauconite samples subjected to higher strain levels (particularly at 40% axial strain) exhibited a slightly

218 greater degree of particle bonding. For these bonded samples, gentle separation was carried out by light finger
219 rubbing and soft brushing to detach agglomerated particles. This procedure has been reported to be effective,
220 introducing no additional particle damage, as the grains are solid and the forces applied by the finger and brush
221 are several orders of magnitude lower than the yielding threshold stress (Suescun-Florez et al., 2020).
222
223 Subsamples, typically containing thousands to tens of thousands of particles (depending on particle size), obtained
224 from the oedometer tests were analyzed using the Microtrac SYNC particle size and shape analyzer. Fig. 5 (a)
225 illustrates the workflow of the Microtrac SYNC particle size and shape analyzer. The sample was dispersed in de-
226 aerated water within the measurement cell, where the flow separated individual particles. Each particle passed
227 through a collimated LED light beam in front of a high-speed digital camera equipped with telecentric optics,
228 minimizing optical distortion and ensuring accurate dimensional measurements.
229
230 Particle size and shape were analyzed simultaneously using the integrated laser diffraction and dynamic imaging
231 modules of the Microtrac SYNC system. The laser diffraction component measured particle size based on the
232 light-scattering patterns generated as particles passed through the laser beam. Detectors positioned at multiple
233 angles recorded the scattering intensity, and the Mie scattering theory (Born and Wolf, 2013) was applied to
234 compute a volume-based particle size distribution and equivalent spherical diameters (e.g., D_{10}, D_{50}, D_{100}). At the
235 same time, the dynamic image analysis module captured two-dimensional grayscale images of thousands of
236 particles per second. These images were processed through intensity thresholding to produce binary (black-white)
237 silhouettes, from which the software automatically extracted each particle's boundary (perimeter, P), projected
238 area (A), and Feret dimensions (FLength and FWidth), as illustrated in Fig. 5 (b).
239

From these primary parameters, the system derived a suite of morphological descriptors, including aspect ratio, sphericity, roundness, and circularity (Fig. 5 (b) and (c)). Shape and size data were computed for all detected particles and statistically averaged by number to characterize the overall particle morphology and size distribution. This dual approach, integrating laser diffraction with dynamic imaging, ensured consistent and validated measurements of both particle size and shape.

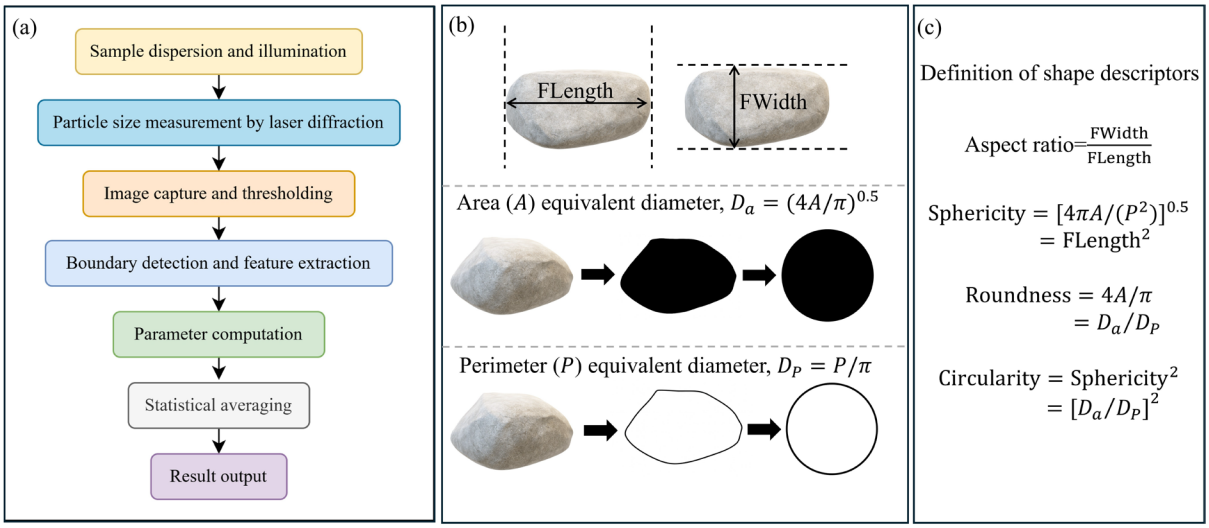

Fig. 4. (a) Workflow of the Microtrac SYNC particle size and shape analyzer integrating laser diffraction and dynamic image analysis; (b) Illustration of geometric parameters used to define the area (A), perimeter (P), Feret Length (FLength) and Feret Width (FWidth); (C) Definitions of shape descriptors, including aspect ratio, sphericity, roundness, and circularity.

3. Results

3.1. Mechanical behaviour of glauconitic and silica sands

3.1.1 Repeatability

Although individual tests on samples with the same glauconite content were subjected to loading and unloading at different axial strain levels, the resulting stress-strain responses and compression planes (Figs. (6)-(9)) exhibit consistent patterns and reasonable reproducibility. The minor scatter observed among tests can be attributed to small variations in initial boundary conditions (e.g., void ratio and seating stress) (Suescun-Florez et al., 2020) and the inherent heterogeneity of the soil, highlighting the inherent difficulty of achieving perfectly identical specimen states and boundary conditions during sample preparation.

3.1.2 Stress-strain response and compression characteristics

This section presents the stress-strain responses and compression characteristics obtained from the oedometer tests. In this study, the mechanical behaviour is illustrated through the stress-strain relationship (axial stress, σ, versus axial strain, ε) and the corresponding compression plane, where the specific volume, $v = 1 + e$, is plotted against σ on a semi-logarithmic scale. The yield point is defined as the inflection point corresponding to the maximum curvature on the compression plane (McDowell and Humphreys, 2002). From this point, the yielding stress σ_y, axial strain at yielding ε_y, and specific volume at yielding v_y are determined, as shown in Figs. (6)-(9) and Fig. 12. On compression plane, the post-yield slope, λ, represents the local gradient of elastic-plastic volumetric strain, while the unloading slope, κ, corresponds to the local gradient of elastic volumetric strain, both obtained by linear fitting (McDowell et al., 1996). For example, for 100% Diest Glauconite (Fig. 6 (b)), λ = -0.58

and κ = -0.02. The threshold plastic work per unit volume when particle crushing commences in one-dimensional compression is calculated as (Huang et al., 2014; Xiao et al., 2019): $W_{th} = \int_0^{\varepsilon_y} \sigma d\,\varepsilon$.

Fig. 6 (a) compares the stress-strain response of 100% Diest glauconite and 100% Vlierzele glauconite under 1D compression tests arrested at approximately 10%, 15-20%, 30% and 40% axial strain. Both materials exhibit broadly similar mechanical behaviour, with nearly overlapping stress-strain curves up to about 30% strain, suggesting comparable stiffness and compressibility. Beyond 30% strain, the Diest glauconite develops silightly higher strength than the Vlierzele glauconite, which may be attributed to its slightly coarser mean particle size or denser packing fabric, promoting more efficient stress transmission and greater resistance to particle rearrangement under large compressive strains. The stress-strain curves display a pronounced concave-upward trend beyond approximately 20% strain, characteristic of strain-hardening behaviour associated with the progressive onset of particle crushing and rearrangement. Such behaviour is consistent with the mechanisms reported by Suescun-Florez et al. (2020) for silica and coral sands tested under similar 1D compression conditions (diameter-to-height ratio 1:1).

Fig. 6 (b) presents the corresponding relationships between specific volume and applied stress for both materials. In each case, the data exhibit a clear bilinear trend in semi-log space, delineating a distinct yielding transition. During the initial loading stage, the specific volume decreases slowly and almost linearly with increasing stress, suggesting an elastic compression regime dominated by particle rearrangement without significant breakage. Once the yield stress is exceeded, the specific volume decreases more rapidly, indicating the onset of particle crushing and progressive fabric densification. Linear fittings to the pre- and post-yield portions of the curves yield transition stresses of approximately 5.16 MPa for Diest glauconite and 5.76 MPa for Vlierzele glauconite. The

294 corresponding work input at yielding is 0.149 MJ/m^3 and 0.184 MJ/m^3 for Diest and Vlierzele glauconite,
295 respectively. The slightly higher yield stress of the Vlierzele sample suggests a more interlocked or resistant fabric,
296 whereas the steeper post-yield slope observed in the Diest sample reflects a greater degree of volumetric
297 compaction associated with its coarser grains and higher strength at large strains. Overall, these differences are
298 minor, and both glauconites display broadly comparable compressibility characteristics.
299

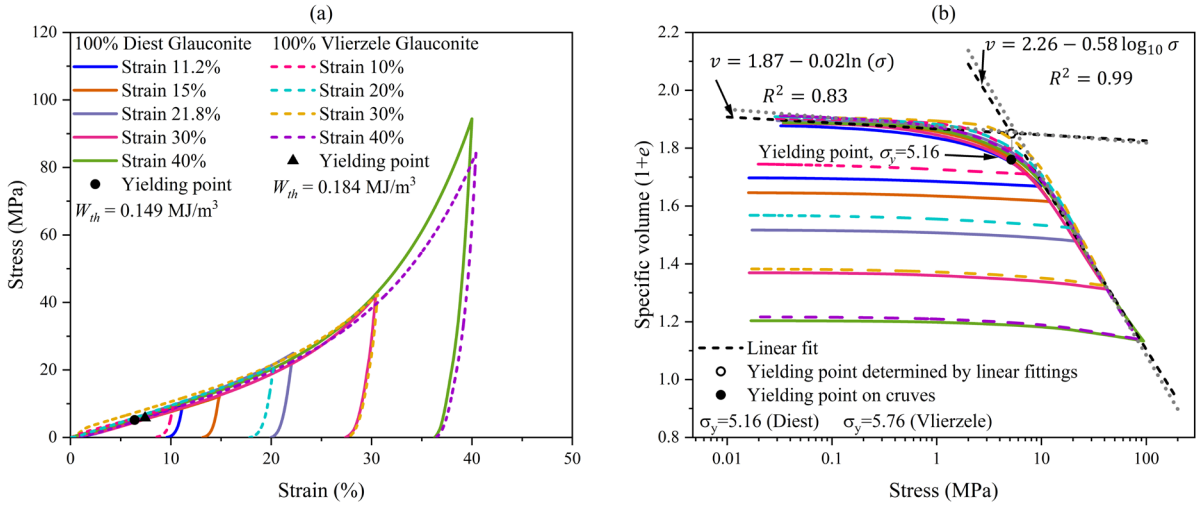

300

301 **Fig. 5**. Comparison between 100% Diest glauconite and 100% Vlierzele glauconite: (a) stress-strain; (b)
302 compression plane.
303

304 Figs. 7 and 8 present the stress-strain and specific volume-stress relationships for the naturally formed Diest and
305 Vlierzele samples, containing 32.4% and 7.8% of glauconite within glauconite-silica sand mixtures, respectively.
306 The overall trends are consistent with those observed for the pure glauconite materials shown in Fig. 6. Both
307 mixtures exhibit a continuous strain-hardening response up to yielding, followed by further strength increase until
308 unloading at the predefined strain levels. Again, the stress-strain curves show concave-up trajectories beyond
309 approximately 20% strain, indicating progressive particle crushing and fabric densification. The corresponding
310 specific volume-stress plots display well-defined bilinear trends in semi-log space, marking distinct yield points.

Limited volumetric change is observed before yielding, followed by rapid compression once particle crushing becomes dominant. The yielding stress increases with decreasing glauconite content, from 6.6 MPa in the natural Diest sample to 10.8 MPa in the natural Vlierzele sample, reflecting the greater load-bearing contribution of the silica grains. Despite the higher yield stress and energy input at yielding in the natural Vlierzele sample (W_{th}=0.289 MJ/m^3) compared with the Diest mixture (W_{th}=0.163 MJ/m^3), both materials display broadly similar compressibility and deformation behaviour, indicating that glauconite content primarily governs the yielding characteristics of these naturally formed sands.

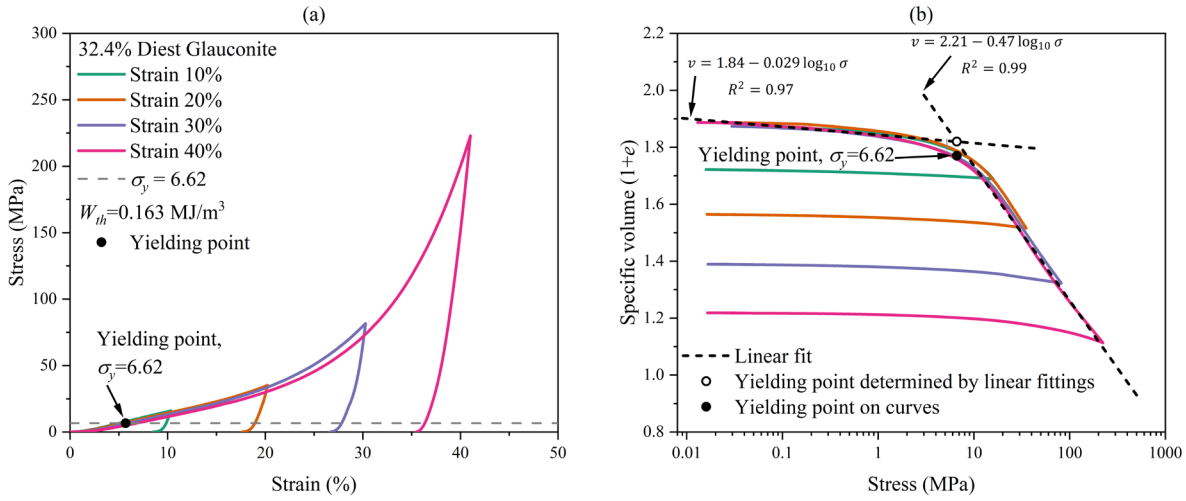

Fig. 6. Naturally formed Diest sample, 32.4% glauconite with 67.6% silica sand: (a) stress-strain; (b) compression plane.

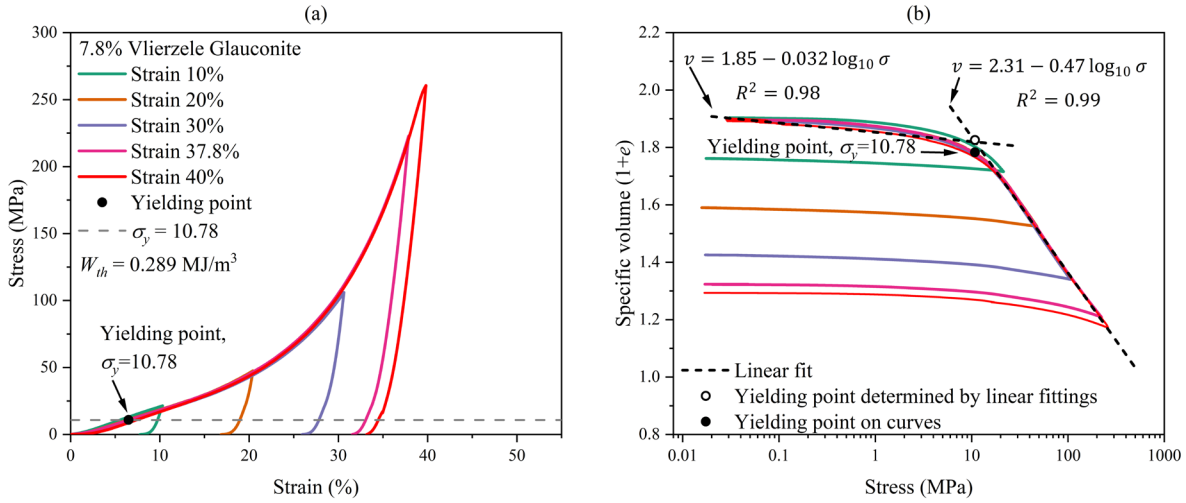

Fig. 7. Naturally formed Vlierzele sample, 7.8% glauconite with 92.2% silica sand: (a) Stress-strain; (b) compression plane.

Fig. 9 presents the stress-strain and specific volume–stress relationships for the 100% silica sand sample under uniaxial compression, together with stress–strain curves for silica sand and coral sand from Florez et al. (2020) for comparison. In Fig. 9 (a), the measured stress-strain response is broadly consistent with previous data reported by Florez et al. (2020) for pure silica sand, although the stress levels observed here are slightly lower than those of their silica sand tests. Fig. 9 (b) shows the corresponding specific volume-stress relationship, which follows a bilinear trend in semi-logarithmic space. The high yield stress, σ_y=14.95 MPa, confirm the strong mechanical strength of silica sand compared with the glauconitic samples. This value falls within the range reported for dry silica sand under 1D compression (σ_y=14-22 MPa) by Nakata et al. (2010). The corresponding work input at yielding (W_{th}=0.319 MJ/m^3) is also notably higher than those of the glauconitic materials (Fig. 6-8), reflecting the greater stiffness and crushing resistance of silica grains.

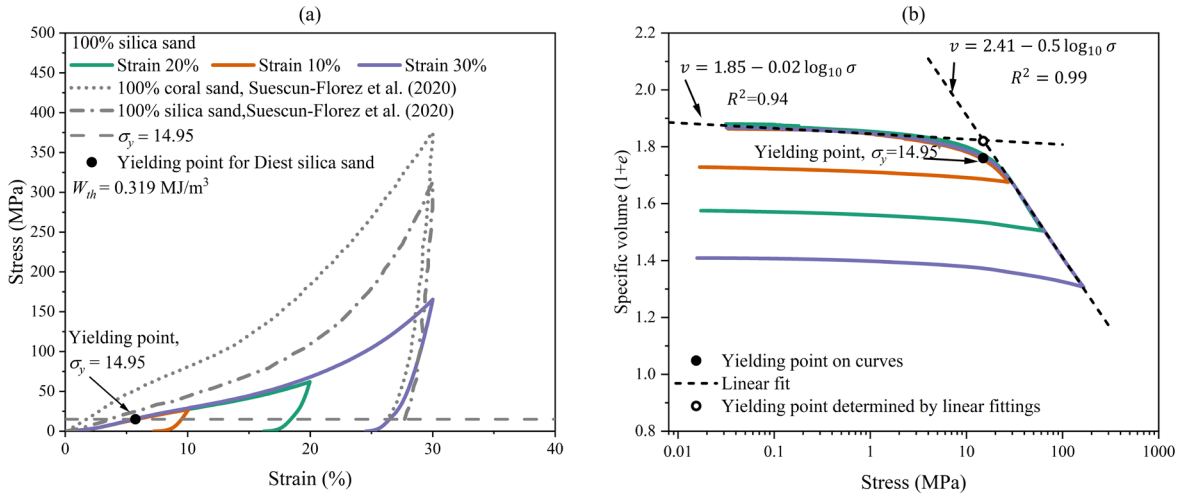

Fig. 8. 100% silica sand: (a) Stress-strain; (b) compression plane.

3.1.3 Influence of glauconite content and material type

Fig. 10 illustrates the influence of glauconite content on the stress-strain responses of glauconite-silica sand mixtures arrested at 30% strain. Fig. 10 (a) shows that the stress-strain curves exhibit systematic variation with glauconite content, where the overall strength and stiffness increase as glauconite content decreases. Samples richer in silica exhibit steeper strain-hardening trends and reach higher stresses, consistent with the greater crushing resistance of silica grains. Fig. 10 (b) presents the corresponding specific volume-stress relationships, which all follow a bilinear trend defining clear yielding transitions. Despite small variations in the initial specific volume, the volumetric strain evolution is similar across the samples, but the post-yield compression curves shift rightward with increasing silica content. The specific volume-stress curve of 100% glauconite reported by Emidio et al. (2009) is also shown for comparison; however, the applied stress level in that dataset was insufficient to clearly identify the yielding stress or post-yield parameters. Fig. 10 (c) quantifies the dependence of yielding stress (σ_y) and work input at yielding (W_{th}) on glauconite and silica contents. Both parameters increase nonlinearly with silica proportion (or decrease with glauconite content), following power-law relationships with high coefficients

of determination (R^2>0.92). These results confirm that mechanical strength and energy absorption capacity are strongly controlled by the mineral composition (glauconite content), with silica-dominated mixtures exhibiting higher stiffness and particle crushing resistance.

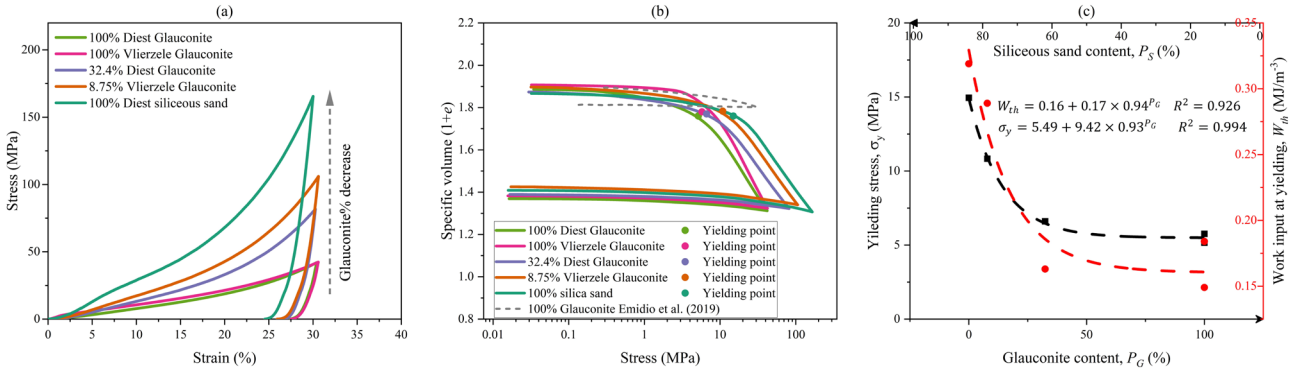

Fig. 9. Influence of glauconite content: (a) stress-strain response up to 30% strain; (b) compression plane; (c) yielding stress and as functions of glauconite/silica content.

3.1.4 Effects of water and loading pattern

Fig. 11 (a) illustrates the stress and strain evolution during the incremental loading (IL) 1D compression test on saturated 100% Diest glauconite (Test 8). Each strain step is followed by a holding period to allow pore pressure dissipation. Fig. 11 (b) presents the corresponding stress-strain relationship, showing a progressive increase in stress with strain, characteristic of strain hardening. The colour scale represents the data point density, increasing from purple (low) to red (high), highlighting the time-dependent accumulation of deformation within each loading stage. When the target strain of each loading step is reached, the system records the current force and maintains it as a constant load. During this adjustment phase, one or two stress fluctuations may occur, causing an increase in strain (typically about 2.5-5%), which results in the discontinuous appearance of the stress-strain curve. Moreover,

when stress is held constant, only the final loading stage exhibits noticeable time-dependent strain (also refer to Fig. 11 (a)), likely reflecting the clay-like behaviour of crushed glauconite under saturated conditions.

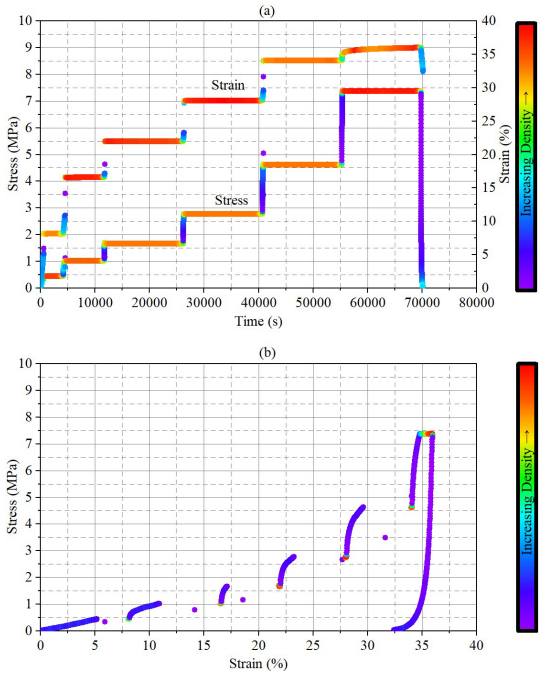

Fig. 10. Demonstration of incremental loading (IL) pattern. (a) stress and strain over time; (b) stress-strain. Colour scale indicates increasing data point density from purple (low) to red (high).

Fig. 12 illustrates the effect of water saturation and loading pattern on the mechanical response of 100% Diest glauconite under 1D compression. Fig. 12 (a) compares the stress-strain behaviour under dry and saturated conditions, using both continuous loading (CL) and incremental loading (IL) modes. The dry sample with CL (Test 5) exhibits the highest stiffness and strength, reaching a yield stress of 5.16 MPa and a peak stress of 94.2 MPa at 40% of strain. In contrast, the saturated samples (Tests 6, 7,8 and 9) show substantially reduced strength, regardless of loading pattern, with yielding stresses of approximately 0.45-0.47 MPa and significantly lower energy input at yielding (W_{th}=0.012-0.013 MJ/m³). The IL tests (Tests 8 and 9) display stepwise strain responses due to load-hold cycles, yet their overall mechanical trends are consistent with the CL results at tested strains. At

386 40% strain, the stress of Test 6 (16.96 MPa) is much lower than that of the dry Test 5, despite both being conducted
387 under CL, indicating that water saturation significantly weakens glauconite. Fig. 12 (b) presents the corresponding
388 specific volume-stress relationships. All curves exhibit the characteristic bilinear trend, with a sharp reduction in
389 specific volume after yielding. The saturated samples show much higher compressibility and lower post-yield
390 stiffness compared with the dry condition. These results demonstrate that water saturation markedly weakens the
391 glauconite structure, reducing its yield stress and energy absorption capacity, while the loading pattern (CL vs IL)
392 exerts a secondary influence on the overall mechanical response.
393

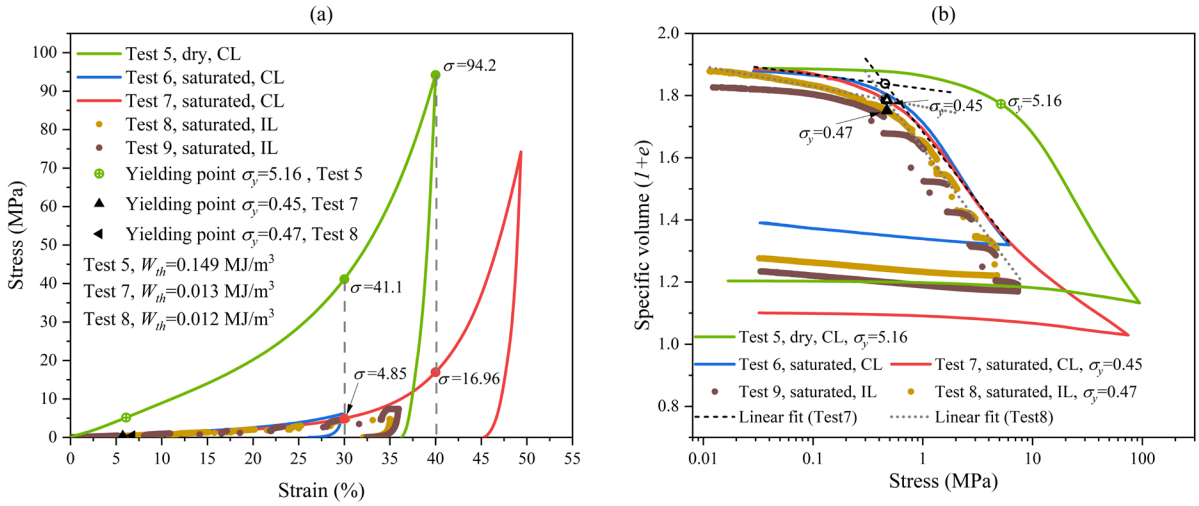

394

395 **Fig. 11**. Effect of water saturation and loading pattern: (a) stress-strain; (b) compression plane.
396

397 Fig. 13 illustrates the effect of water saturation on the mechanical behaviour of 100% silica sand under 1D
398 compression. Fig. 13 (a) compares the stress-strain responses of the dry (Test 25, CL) and saturated (Test 26, IL)
399 samples. Both show similar yielding stresses (σ_y≈14.5-14.95 MPa), but the dry specimen exhibits higher stiffness
400 and strength, reaching a peak stress of 165.6 MPa at 30% of strain, while the saturated sample attains only 107
401 MPa. Fig. 13 (b) presents the corresponding specific volume-stress relationships, both exhibiting bilinear trends

with distinct yield points and similar post-yield slopes of -0.50 and -0.51, respectively. A comparison between Fig. 12 and Fig. 13 shows that water saturation reduces the stress of 100% silica at 30% strain by 35.3%, whereas the reduction for 100% Diest glauconite reaches 88.2%, highlighting the markedly higher water sensitivity of glauconitic material.

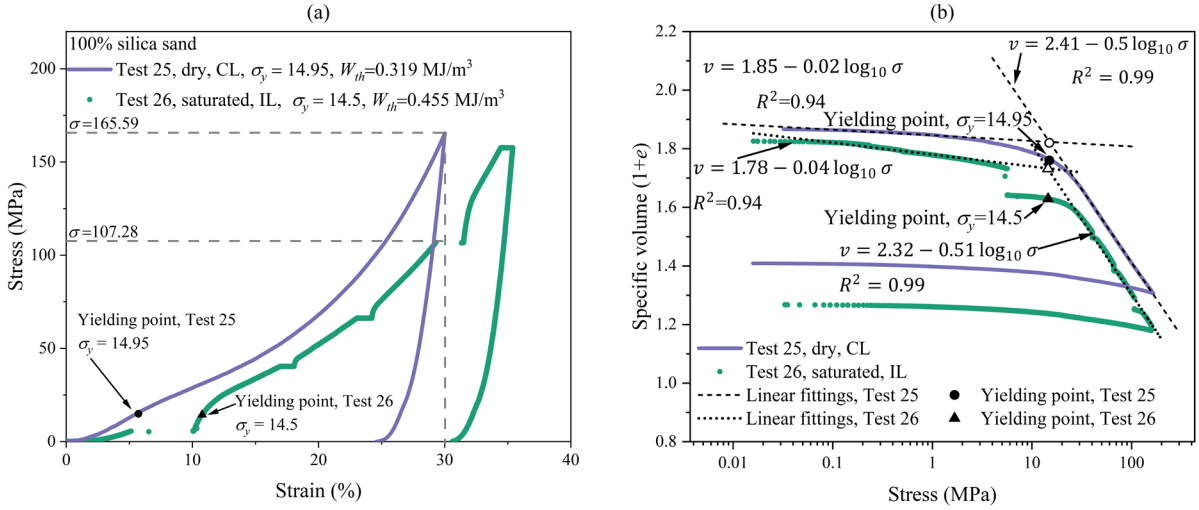

Fig. 12. Effect of water on 100% silica sand: (a) stress-strain; (b) compression plane.

These results align with previous studies showing that water weakens the strength of soils under one-dimensional compression (Miura and Toyotoshi, 1975; Ham et al., 2010; Wils and Haegeman, 2014). This behaviour has been attributed to water accelerating particle crushing and enhancing compressibility by reducing surface energy and weakening particle asperities. The pronounced strength loss and increased compressibility observed in saturated glauconite are therefore consistent with the general weakening trend reported for other crushable soils, although the underlying mechanisms require further investigation. In contrast,, Cavarretta et al. (2010) that water had little effect on the crushing of ballotini glass beads, and attributed this to the material's strong silica composition and smooth, non-porous surfaces. This contrast indicates that the influence of water on particle breakage is highly

418 mineral-dependent, being significant for weak, micro-porous minerals such as glauconite but relative minor for
419 dense, silica-rich materials.
420
421 ***3.2. Microscopic and particle-scale observation of the crushing process***
422 Fig. 14 shows stereomicroscope photographs illustrating the progressive crushing of 100% Diest glauconite, 32.4%
423 Diest glauconite, and 100% silica sand arrested at different strain levels. All three materials exhibit a similar
424 progression of particle breakage, with gradual surface abrasion and generation of finer fragments as strain or stress
425 increases, consistent with the observations of Suescun-Florez et al. (2020) for silica sand and Xiao et al. (2019)
426 for carbonate sand. At 10-20% strain, only minor surface abrasion is visible, whereas more pronounced
427 fragmentation appears beyond 30% strain. However, the extent of breakage at 30% strain differs among materials:
428 the 32.4% Diest glauconite and 100% silica sand samples show more severe crushing and finer debris formation,
429 whereas the 100% Diest glauconite largely retain original morphology but with significant surface abrasion. These
430 observations suggest that while the overall breakage mechanism is similar, the degree of particle damage depends
431 on mineral composition and grain strength. For all materials, very few particles appear to have survived
432 undamaged at largest strain level, indicating that the maximum particle size may decrease. This observation
433 contrasts with Suescun-Florez et al. (2020), who reported that a few larger silica grains remained intact at 30%
434 strain, likely due to their more angular morphology and higher crushing resistance.
435
436 Fig. 15 shows representative 2D particle projections at d_{90}, d_{50} and d_{10} for 100% Diest Glauconite and 100%
437 silica sand arrested at different strain levels. Both materials display progressive particle size reduction with
438 increasing strain, reflecting continuous crushing and the generation of fines. Larger particles (d_{90}) remain
439 relatively intact up to 20% strain but become noticeably smaller and more irregular beyond 30%. Finer fractions

(d_{50} and d_{10}) show rapid fragmentation, indicating preferential breakage of smaller grains (Coop et al., 2004; Russell and Muir Wood, 2009; McDowell and De Bono, 2013). However, silica sand shows a slightly greater degree of size reduction than glauconite at 30% strain, consistent with its higher brittleness and the greater stresses reached during compression.

Fig. 16 presents the microscopic evidence of particle breakage mechanisms in saturated 100% Diest Glauconite subjected to uniaxial compression (Test 8). The vertical slice extracted from the mid-plane of the specimen (Fig. Fig. 16 (a) and (b)) for polarized-light micrographs. Localized micrographs (Fig. 16 (c)) reveal three dominant modes of particle breakage (as schematically illustrated in Fig. 16 (d)): (i) abrasion/chopping, characterized by surface polishing and edge chopping (red dashed ellipses); (ii) splitting, manifested as splitting failures of elongated particles along weak planes (blue dashed ellipses); and (iii) crushing/comminution, marked by extensive internal cracking and grain pulverization (green dashed ellipses). These features indicate the coexistence of multiple breakage mechanisms, ranging from surface abrasion to complete fragmentation, governed by individual particle strength and the local force network within the granular packing. This behaviour is consistent with crushing patterns commonly reported for granular geomaterials (Nakata et al., 2001; Einav, 2007a; Zhao et al., 2020; Wang et al., 2026).

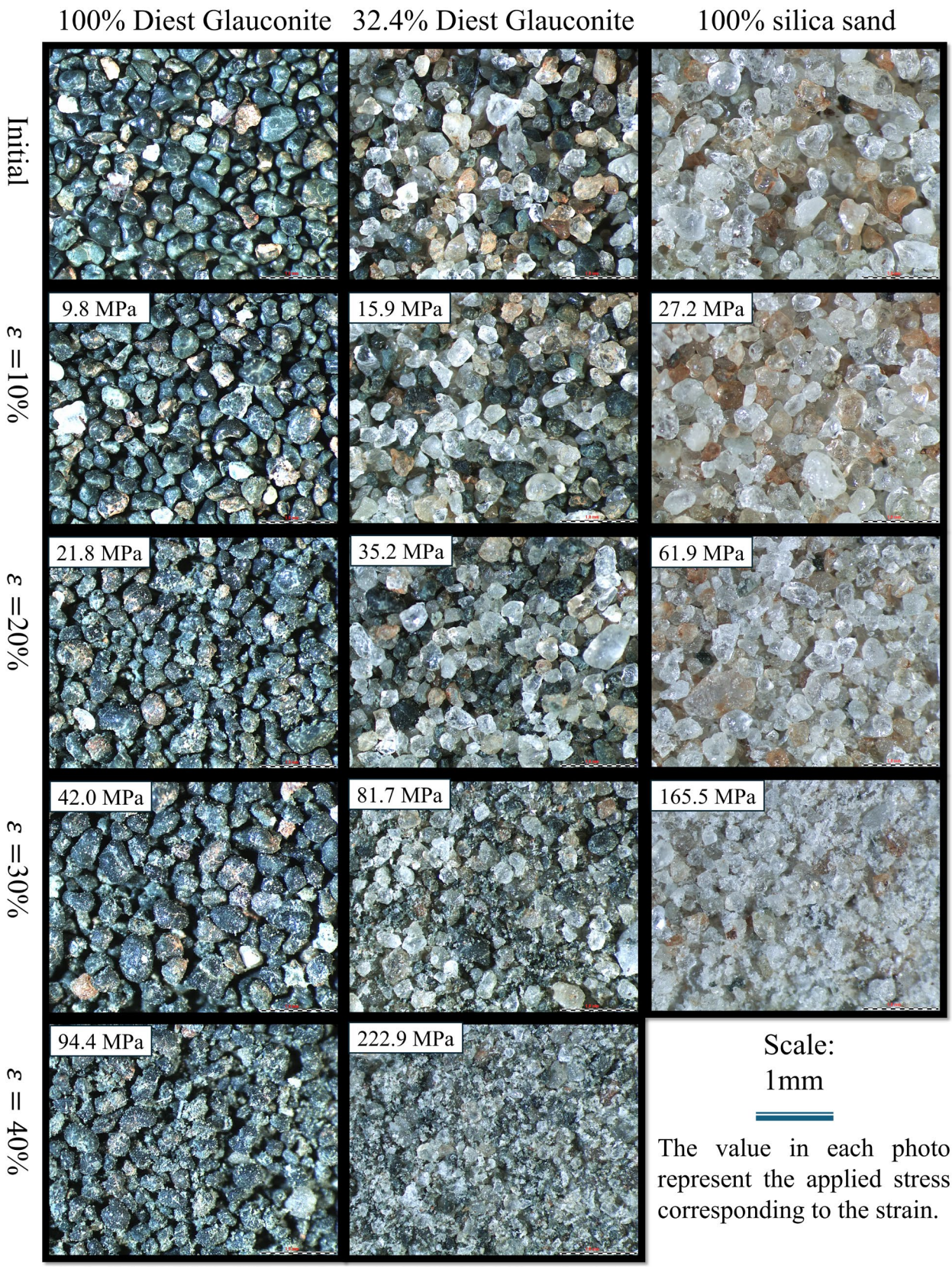

Fig. 13. Stereomicroscope photographs illustrating the progressive crushing of 100% Diest Glauconite, 32.4% Diest Glauconite, and100% Diest silica sand arrested at different strain levels.

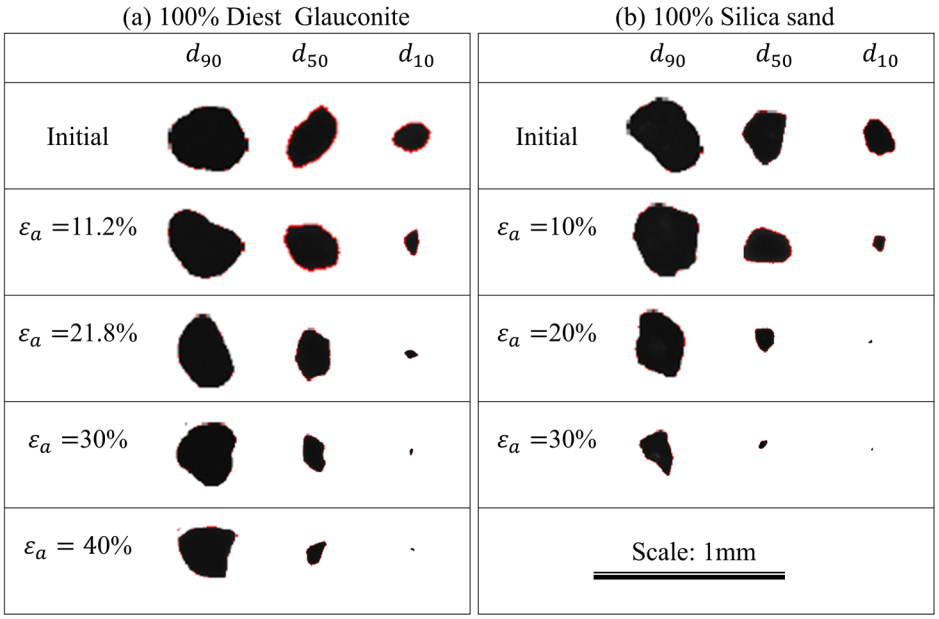

460

461 **Fig. 14.** Representative particle shapes at d_{90}, d_{50} and d_{10} with increasing axial strain for (a) 100% Diest

462 Glauconite and (b) 100% silica sand.

463

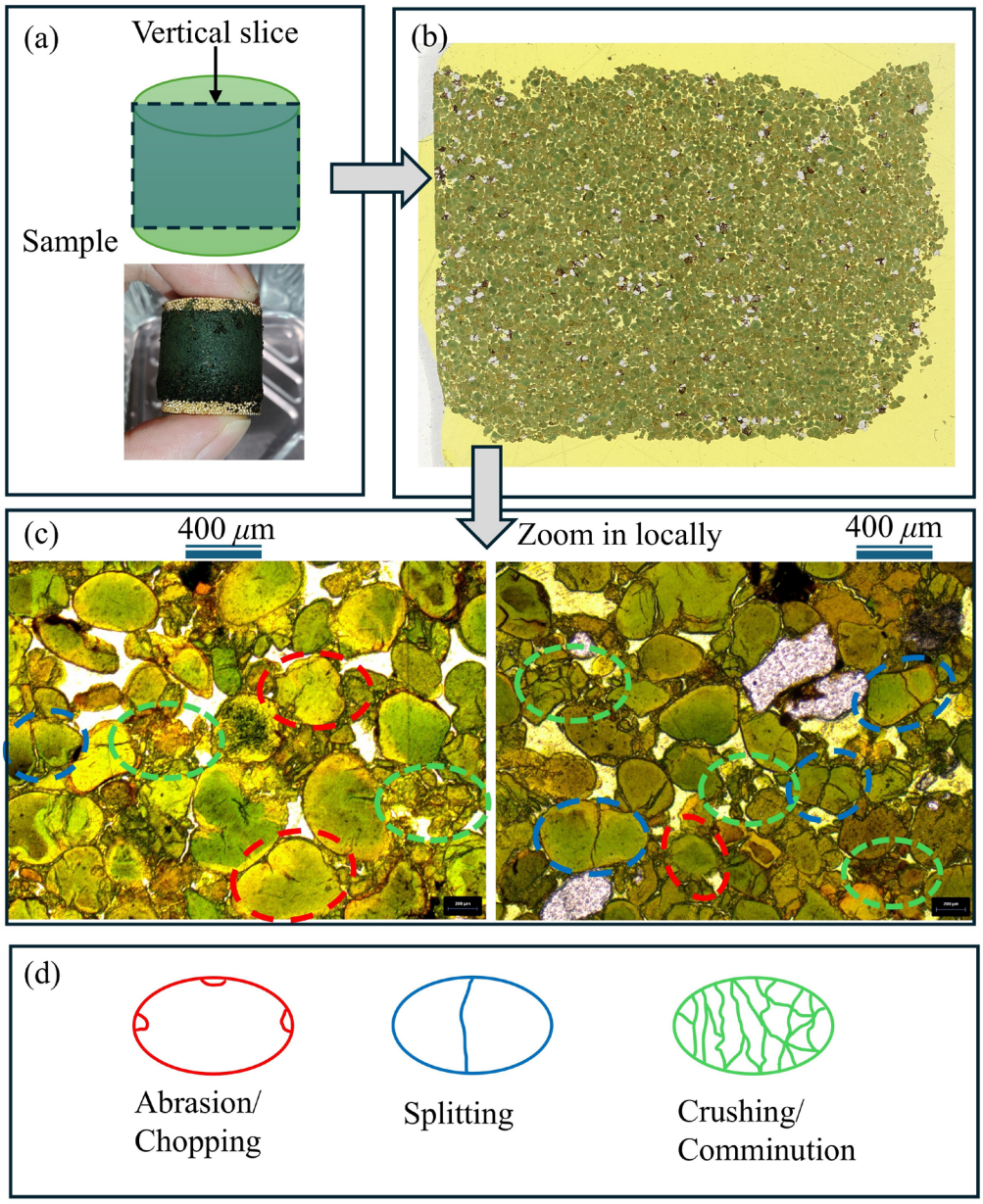

Fig. 15. Microstructural observations of glauconite grains after uniaxial compression. (a) Cylindrical specimen and schematic of the vertical slice used for microscopy. (b) Cross-sectional micrograph of the polished slice. (c) Polarized-light micrographs showing typical grain-scale damage: abrasion, splitting, and crushing. (d) Schematic illustration of the three dominant breakage modes: abrasion/chopping (red), splitting (blue), and crushing/comminution (green).

3.3. Quantitative analysis of particle size evolution

This section presents the PSDs obtained from 1D compression tests on dry glauconite-silica mixtures arrested at different strain levels. Several parameters based on PSD evolution have been proposed to characterize grading changes, such as breakage index (Hardin, 1985), the grading state index (Muir Wood, 2007), relative breakage index (Einav, 2007b) and modified grading state index (reference). These parameters share the same underlying principle: each quantifies grading evolution by measuring the positional shift of the PSD curve relative to reference states. In this study, the evolution of the PSDs is quantified using the relative breakage index (Einav, 2007b) to facilitate direct comparison with existing literature. Another parameter, the fractal dimension of PSD, is also introduced and will be explained later.

Fig. 17 illustrates the definition of the index of relative breakage B_r proposed by Einav (2007b):

$$B_r = \frac{B_t}{B_p} = \frac{\text{Area}(ACDG)}{\text{Area}(ACEF)} \tag{1}$$

where B_t is the total breakage, defined as the area between the initial PSD and the current PSD $\text{Area}(ACDG)$, and B_p is the breakage potential, defined as the area between the initial PSD and ultimate fractal PSD $\text{Area}(ACEF)$. The ultimate fractal PSD curve can be expressed as (reference):

$$P_m(d < d_s) = 100\left(\frac{d_s^{3-D_{su}} - d_{sumin}^{3-D_{su}}}{d_{sumax}^{3-D_{su}} - d_{sumin}^{3-D_{su}}}\right) \tag{2}$$

where d is the particle size, d_s is the particle size corresponding to a given point on the PSD curve, and D_{su}, d_{sumin} and d_{sumax} denote the fractal dimension, and the minimum and maximum particle size of the ultimate fractal PSD, respectively. The concept of the relative breakage is essentially the same as the grading state index proposed by Muir Wood (2007) and the modified grading state index (reference),

If the current PSD follows a fractal distribution, it can be expressed as:

493 $$P_m(d < d_s) = 100\left(\frac{d_s^{3-D_s} - d_{scmin}^{3-D_s}}{d_{scmax}^{3-D_{su}} - d_{scmin}^{3-D_{su}}}\right) \quad (3)$$

494 where D_s, d_{scmin} and d_{scmax} denote the fractal dimension, and the minimum and maximum particle size of the

495 current fractal PSD, respectively.

496

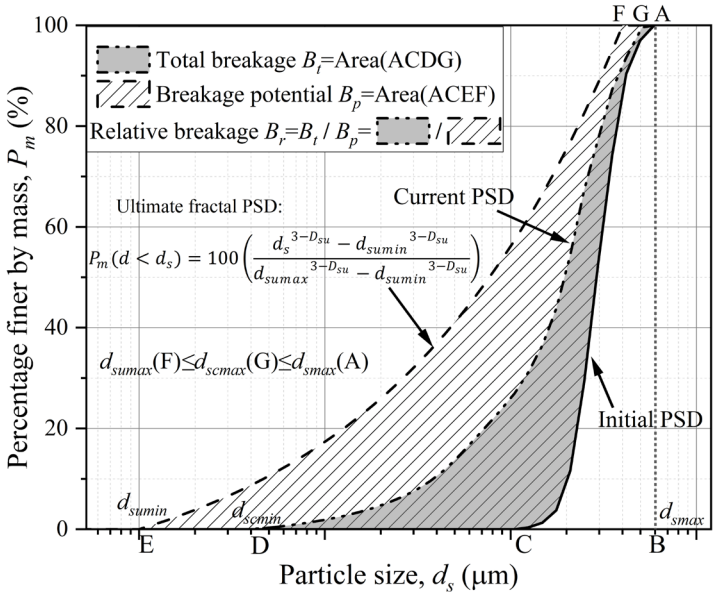

497

498 **Fig. 16.** Definition of relative breakage (Einav, 2007b).

499

500 3.3.1 Evolution of particle size distribution and relative breakage

501 Fig. 18 shows the evolution of PSDs and corresponding relative breakage (B_r) for dry glauconite-silica mixtures

502 arrested at different axial strains. In Fig. 18 (a)-(e), all samples exhibit a systematic shift of the PSD curves toward

503 finer sizes with increasing strain, indicating continuous particle breakage. It can be noted that both the maximum

504 and minimum particle sizes evolve with strain, consistent with previous observations (Wils and Haegeman, 2014;

505 Manso et al., 2018; Suescun-Florez et al., 2020; Jiang et al., 2026). Specifically, the minimum particle size of 100%

506 glauconite decreases to approximately 1 μm, while that of the glauconite-silica mixtures and 100% silica sand

507 reaches about 0.5 μm. The most significant reduction in maximum particle size is observed in 100% silica sand,

508 from 497 μm to 296 μm.

509

510 Some studies, however, have reported that the maximum particle size remains largely unchanged during crushing,
511 as larger grains generally possess more contact points and higher coordination numbers, resulting in lower average
512 contact forces and, consequently, reduced breakage probability (McDowell and Bolton, 1998; Ciantia and
513 O'Sullivan, 2020). Accordingly, several researchers have reported that the maximum particle size remains
514 effectively constant when calculating relative breakage (Huang et al., 2014; Xiao et al., 2017). In contrast, the
515 results in this study suggest that even the coarser silica grains underwent noticeable size reduction, likely due to
516 the high applied stress levels (Wils and Haegeman, 2014; Manso et al., 2018; Suescun-Florez et al., 2020).
517 Therefore, it is reasonable to assume that $d_{sumax} \leq d_{scmax} \leq d_{smax}$, where d_{smax} denotes the maximum particle
518 size of the initial PSD, as illustrate in Fig. 17.

519

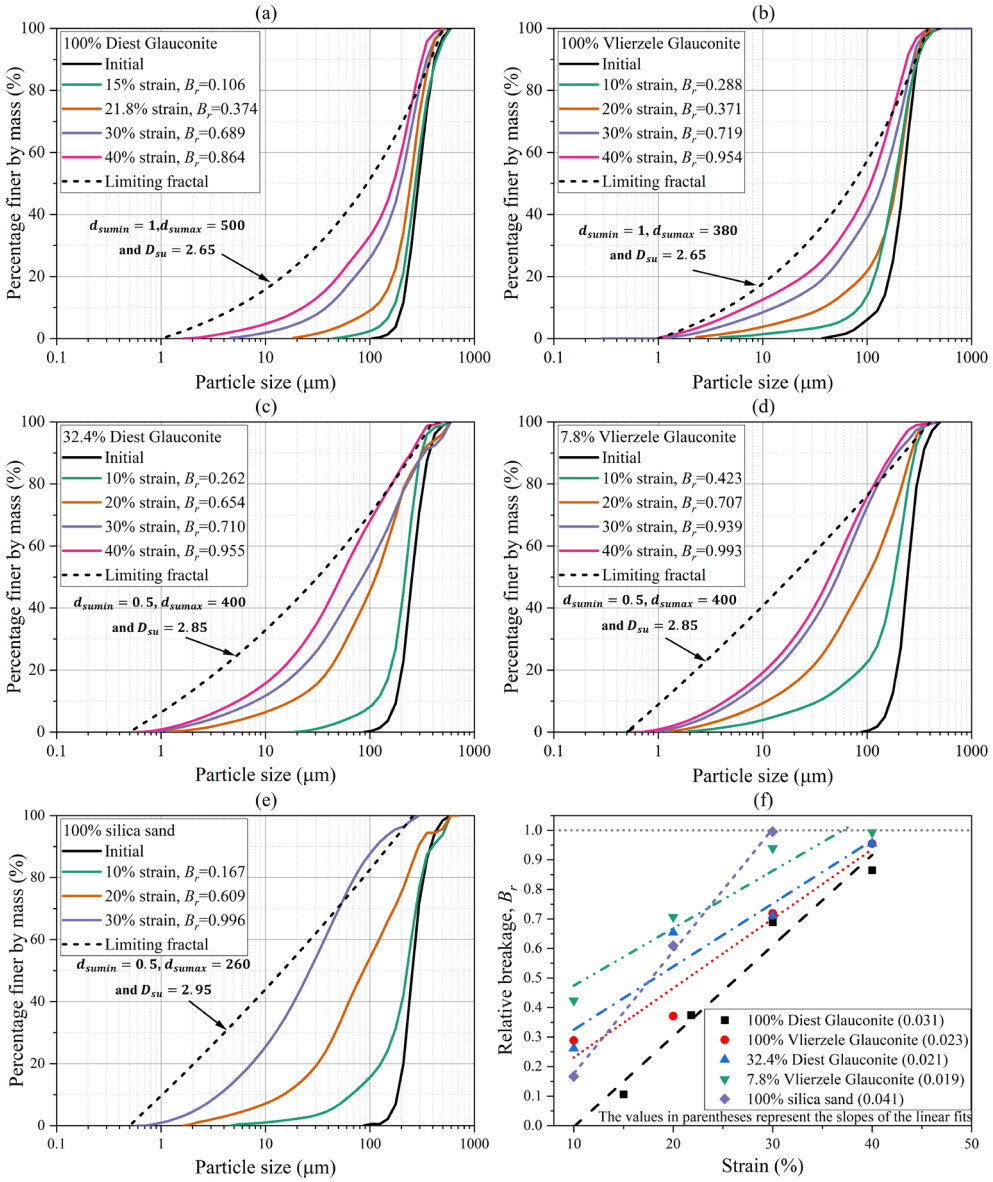

Fig. 17. Evolution of particle size distributions and the relative breakage. (a) 100% Diest glauconite; (b) 100% Vlierzele glauconite; (c) 32.4% Diest glauconite; (d) 7.8% Vlierzele glauconite; (e) 100% silica sand; (f) relative breakage plotted against strain.

For most soils formed by fragmentation or crushing processes, the ultimate fractal dimension D_{su} typically ranges between 2.3 and 2.95 (Perfect, 1997; McDowell and Bolton, 1998; Coop et al., 2004; Russell, 2010; Huang et al., 2017; Li et al., 2022). However, soils produced by other geological mechanisms may exhibit D_{su} values outside this range. For example, Storti et al. (2003) reported that the fractal dimension of fault gouge increases from 1.8

529 to 3.6 as the sampling area approaches the shear band. In this study, the value of ultimate fractal dimension is
530 inferred based on two considerations: (i) it should not be smaller than the maximum fractal dimension measured
531 experimentally, and (ii) it should remain consistent with the observed trend of progressive particle crushing. The
532 values of d_{sumin} and d_{sumax} were taken from the minimum and maximum measured values, respectively.
533 Accordingly, the assumed D_{su} values satisfy the above criteria. All values and the corresponding calculated B_r
534 are listed in the Fig. 18 (a)-(e).

535

536 Fig. 18 (f) shows the relationship between B_r and axial strain. B_r increases linearly with strain, consistent with
537 the observations of Yu (2017) and Wu et al. (2020) on silica sands, with steeper slopes indicating greater breakage
538 rates. Among the samples, 100% silica sand exhibits the greatest breakage rate (B_r/ε).

539

540 3.3.2 Evolution of fractal dimension

541 Many studies have shown that PSD of granular materials progressively evolves toward a fractal form during
542 particle crushing, with fractal dimension increasing as crushing progresses (McDowell et al., 1996; Russell, 2011;
543 Xiao et al., 2016; Huang et al., 2017; Yao et al., 2023). As shown in Fig. 19 (a), the PSDs of 100% Diest Glauconite
544 at different axial strains become progressively finer and linear in log-log space, reflecting the development of a
545 fractal distribution. Particle sizes larger than the effective particle size (d_{10}) were used in linear fitting. The slopes
546 of the fitted lines ($3 - D_s$) yield fractal dimensions that increase from D_s=0.289 at ε=15% to D_s=2.178 at ε =40%.

547

548 Fig. 19 (b) presents the variation of D_s with strain. The data were fitted using an asymptotic function, as shown in
549 the figure. All materials exhibit a rapid initial increase in fractal dimension that gradually approaches an upper

limit D_{su}, corresponding to the ultimate fractal state. The fitted parameters (shown in parentheses) demonstrate excellent correlation (R^2>0.9) for all cases. Overall, the results confirm that particle crushing drives the PSD toward a stable fractal form, with both the rate of evolution and the ultimate fractal dimension dependent on mineral type and initial grading.

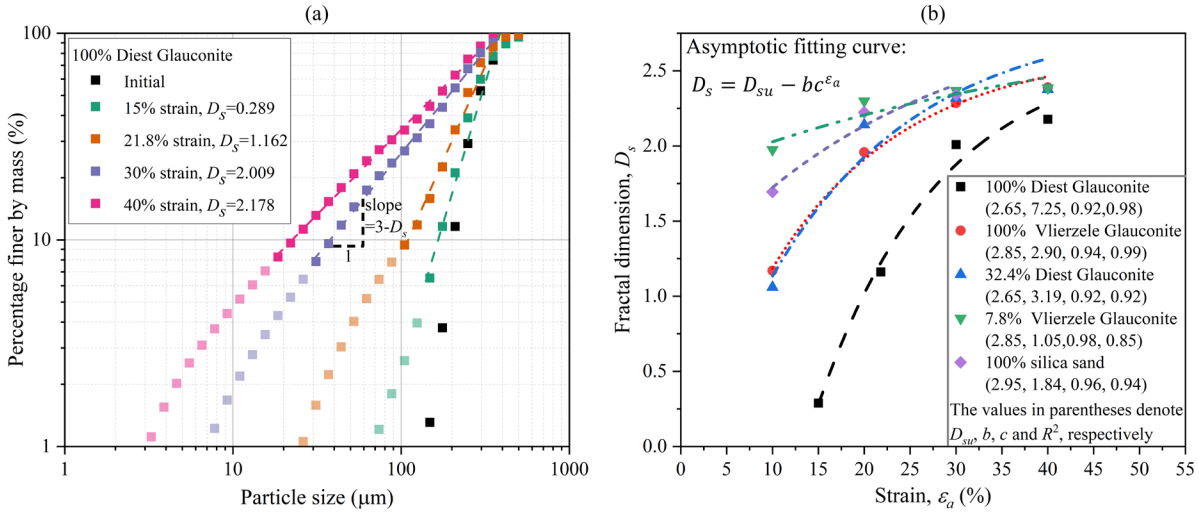

Fig. 18. (a) Example of determining the fractal dimension D_s; (b) evolution of fractal dimension with strain.

Fig. 20 shows the relationship between B_r and D_s for different glauconite-silica mixtures. In all cases, B_r increases nonlinearly with D_s, following an exponential trend expressed as:

$$B_r = ne^{(D_s/m)+\beta} \quad (4)$$

where n, m, and β are fitting parameters. The fitted curves exhibit high coefficients of determination (R^2>0.85). Huang et al. (2017) reported a linear the relationship between B_r and D_s for quartz sand. This difference reflects material-dependent breakage behaviour. Quartz tends to crush progressively and proportionally, whereas glauconite-rich mixtures undergo more abrupt fragmentation once breakage initiates. The exponential form therefore captures the accelerated increase in fractal dimension associated with the rapid fragmentation of these weaker minerals.

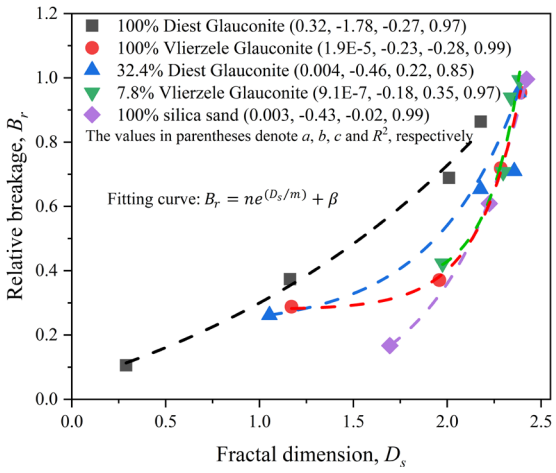

Fig. 19. relationship between relative breakage and fractal dimension

3.4. Relationships between energy dissipation, stress, relative breakage and fractal dimension

To integrate the two key factors influencing particle breakage, i.e., stress and strain, the concept of specific plastic work is adopted to evaluate the energy dissipation during the particle breakage process. The specific plastic work done per unit volume can be calculated as follows (Huang et al., 2014; Xiao et al., 2019):

$$W = W_{th} + \int_{\varepsilon_y}^{\varepsilon} \sigma \mathrm{d}\varepsilon \tag{5}$$

where σ and ε are the axial stress and strain, respectively, and ε_y is the axial strain at yielding. $W_{th} = \int_0^{\varepsilon_y} \sigma d\,\varepsilon$ represents the threshold plastic work per unit volume when particle crushing commences in 1D compression test. The values of W_{th} for each tests are presented in Fig. 6-9 and Fig. 12.

Fig. 21 (a) presents the relationship between specific work and stress for 1D compression tests on dry samples containing different amounts of glauconite. Linear regression yields an R^2 value of 0.991 for the reported tests. Fig. 21 (b) shows the relationship between relative breakage and stress. Huang et al. (2014) proposed a theoretical relationship between stress and relative breakage, given as:

584 $$B_r = \omega \ln\left(\frac{\sigma}{\sigma_y}\right) \quad (6)$$

585 where ω is a fitting coefficient. Equation (6) was applied to each set of experimental data, resulting in an average
586 R^2 value of 0.860. Alternative fitting forms, such as the logistic model, have also been used by other researchers
587 (Li et al., 2022).

588

589 Fig. 21 (c) presents the relationship between relative breakage and specific work. The relationship between B_r
590 and W proposed by Huang et al. (2014) can be expressed as:

591 $$B_r = \xi \ln\left(1 + \frac{W - W_{th}}{W_0}\right) \quad (7)$$

592 where $W_0 = \sigma_y \Lambda(-v_y^{-1})$ represents the characteristic plastic work dissipated in the particle breakage process, v_y
593 is the specific volume at yielding and $\Lambda = \lambda - \kappa$, ξ is a material constant. When Equation (7) was applied to each
594 dataset in Fig. 21 (c), low R^2 values were obtained. Fitting all experimental data together yields an R^2 value of
595 0.879. However, this formulation may yield B_r>1, as shown in Fig. 21 (c), which is mathematically inconsistent
596 with the definition of relative breakage. To overcome this limitation, an alternative relationship was developed:

597 $$B_r = 1 - e^{\left(-\xi \ln\left(\frac{W+a}{W_{th}}\right)\right)} \quad (8)$$

598 Or equivalently,

599 $$B_r = 1 - \left(\frac{W_{th}}{W+a}\right)^{\xi} \quad (9)$$

600 where a is a fitting parameter. The logarithmic term $\alpha \ln\left(\frac{W+a}{W_{th}}\right)$ is derived from Equation (6) by substituting stress
601 with specific work, since a linear relationship between stress and specific work was observed (as reported in Fig.
602 21 (a)). The best fit of Equation (9) (R^2=0.901) gives:

603 $$B_r = 1 - \left(\frac{32.59}{33.03+W}\right)^{7.58} \quad (10)$$

604 In this expression, B_r asymptotically approaches 1 as W increases. This form effectively captures the nonlinear
605 growth behaviour associated with energy dissipation and particle breakage observed in this study.

606

607 Fig. 21 (d) shows the relationship between fractal dimension D_s and specific work W for tests on dry samples
608 with varying glauconite content. The results show that D_s increases rapidly with increasing W at low specific
609 work levels, followed by a gradual approach to an asymptotic value (ultimate fractal dimension D_{su}) as W
610 continue to increase. The data are represented by an exponential function:

611 $$D_s = 3(1 - e^{-0.42W}) \quad (11)$$

612 This indicates that the fractal dimension tends to stabilize near 3 at very high specific work levels, suggesting that
613 particle fragmentation becomes progressively limited once most crushable grains have failed and additional
614 energy is dissipated primarily through bond formation or surface rearrangement. The consistent trend across
615 samples with varying glauconite contents implies that the evolution of particle size distribution with increasing
616 energy input follows a similar fractal pattern, largely independent of glauconite proportion.

617

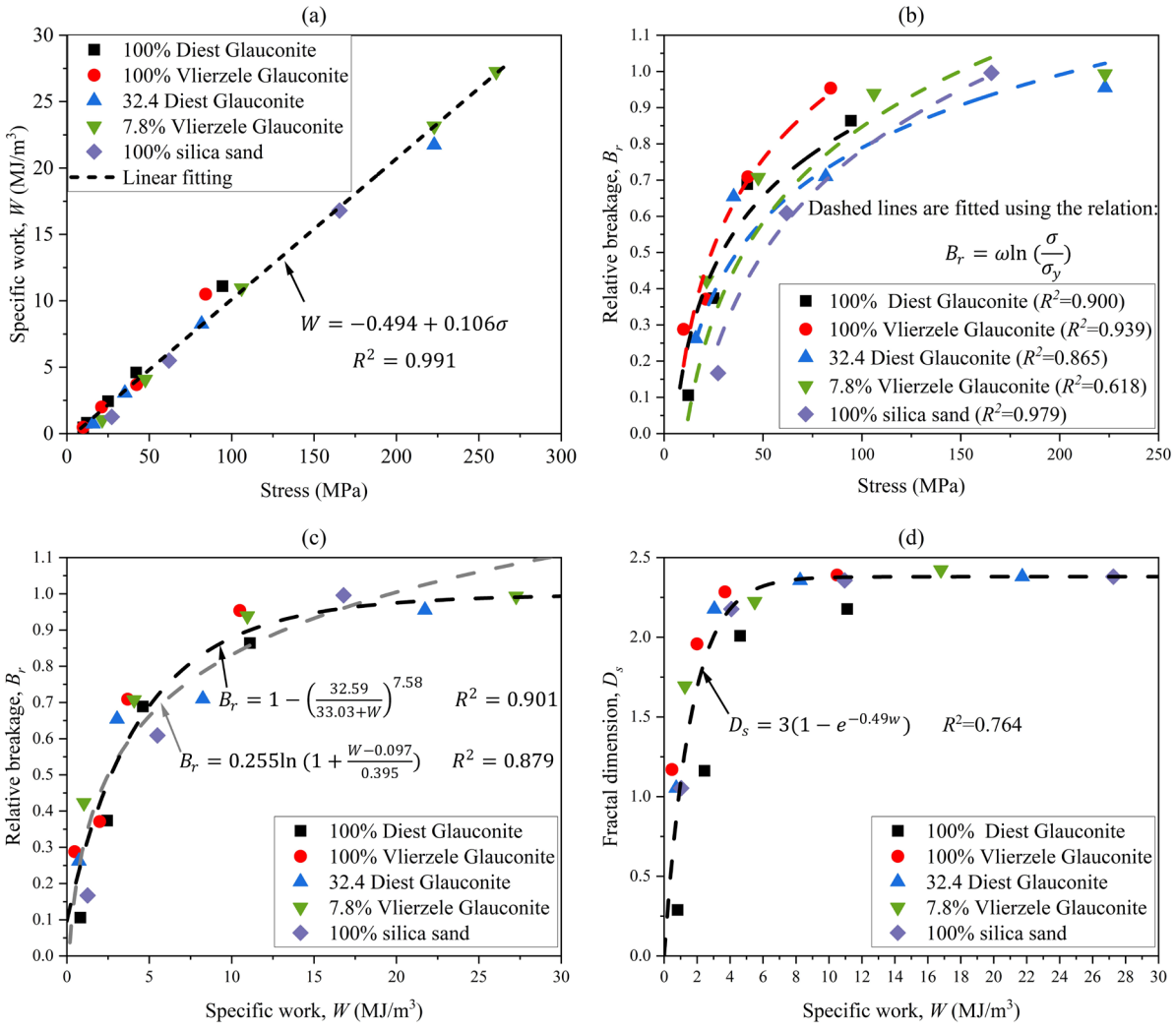

Fig. 20. (a) Specific work plotted against stress; (b) relative breakage plotted against stress; (c) relative breakage plotted against specific work; (d) fractal dimension plotted against specific work.

3.5. Particle shape evolution

The evolution of particle shape descriptors (i.e., aspect ratio, sphericity, roundness and circularity) with increasing relative breakage is shown in Fig. 22. The values of each shape descriptor were obtained by averaging measurements from thousands to tens thousands of individual particles. To describe the evolution of mean aspect ratio α with relative breakage B_r, the theoretical relationship proposed by Buscarnera and Einav (2021) is aslo considered here. They introduced a mathematical expression that links between particle breakage to shape

628 evolution through aspect ratio:

629 $$\alpha = \alpha_L + (\alpha_0 - \alpha_L)e^{-C_\alpha(B/(1-B))} \quad (12)$$

630 where B is a breakage internal variable, which is a particular form of the relative breakage B_r (Einav, 2007b); α_0
631 is the aspect ratio prior to breakage; C_α is a constant controlling the rate of shape evolution in relation with the
632 breakage growth rate; and α_L is the ultimate value of α.

633

634 Fig. 22 (a) shows the relationships between the aspect ratio α and the relative breakage for samples with varying
635 glauconite contents under dry testing condition. In all cases, the aspect ratio decreases with increasing B_r,
636 indicating that particles become more elongated as breakage progresses. The relationship is well described by
637 Equation (12). The fitting results show excellent agreement with the experimental data, with coefficients of
638 determination (R^2) ranging from 0.937 to 0.991. The initial aspect ratio α_0 and the ultimate aspect ratio α_L vary
639 slightly among the samples, reflecting differences in initial particle morphology and resistance to shape change.
640 Samples containing glauconite generally exhibit higher α_L values compared with silica sand, suggesting that
641 glauconitic grains tend to retain more equant shapes during breakage.

642

643 Fig. 22 (b)-(f) show the evolution of shape descriptors, i.e., aspect ratio, mean sphericity, roundness, and circularity,
644 with increasing relative breakage B_r for the five tested materials. In all cases, the aspect ratio and roundness
645 decrease gradually as breakage progresses, by 3.4-8.4% and 4.0-9.3%, respectively, indicating that particles
646 become more elongated and irregular with increasing fragmentation. The reductions in sphericity (0.8-1.8%) and
647 circularity (0.9-3.6%) are less pronounced, suggesting that breakage primarily modifies particle elongation rather
648 than overall smoothness of the particle outline. Among the materials, glauconitic samples generally exhibit higher
649 values of aspect ratio and sphericity compared with silica sand, again reflecting their tendency to obtain more

650 equant shapes during crushing.

651

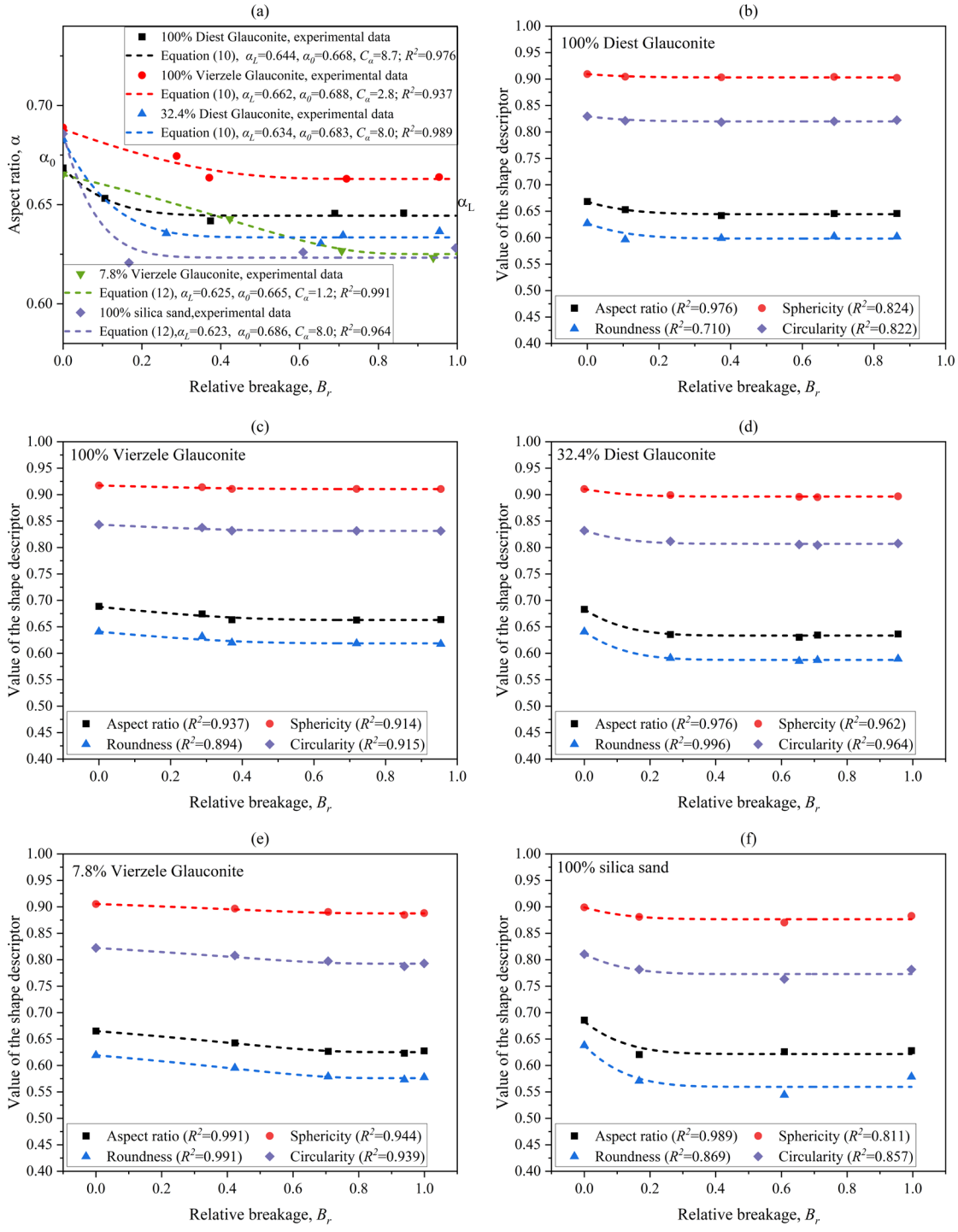

652

653 **Fig. 21.** (a) Relationship between mean aspect ratio and relative breakage for the tested samples; (b-f) Variations

654 of shape descriptors with relative breakage for (b) 100% Diest Glauconite, (c) 100% Vlierzele Glauconite, (d)

655 32.4% Diest Glauconite, (e) 7.8% Vlierzele Glauconite, and (f) 100% silica sand.

Equation (12) was further applied to fit the evolution of these shape descriptors, showing excellent agreement with the experimental data, with coefficients of determination (R^2) ranging from 0.71 to 0.99. These results confirm that Equation (12) can be extended and effectively capture the observed trends in particle shape evolution. A modified form of Equation (12) can be expressed as:

$$s = s_L + (s_0 - s_L)e^{-C_\alpha(B_r/(1-B_r))} \quad (13)$$

where s represent a shape descriptor (i.e., aspect ratio, sphericity, roundness, or circularity), s_0 is the initial value and s_L is an ultimate value.

To better understand the mechanisms underlying the reduction in mean aspect ratio shown in Fig. 22 (a), Fig. 23 presents the relative frequency distributions of aspect ratio α for all tested materials. These distributions, based on tens of thousands of particle measurements with a bin size of 0.05, reveal how the proportions of elongated and equant particles evolve with increasing relative breakage. Each distribution is unimodal, with the peak generally located around α=0.6-0.72, corresponding to sub-elliptical to sub-equant particles.

For the 100% Diest Glauconite sample (Fig. 23 (a)), the most pronounced change in relative frequency occurs between the initial state and the first breakage level (B_r=0.106). This stage is characterized by a reduction in the proportion of nearly equant particles ($\alpha \geqslant 0.775$) and a corresponding increase in elongated particles ($\alpha \leqslant 0.725$). With further breakage (B_r=0.374-0.864), the distributions remain almost unchanged, indicating that most shape modification occurs during the earliest phase of crushing. This observation is consistent with the relationship between mean aspect ratio and relative breakage as shown in Fig. 22 (a). The initial mean aspect ratio, α_0=0.668, and the ultimate mean aspect ratio, α_L=0.644 are indicated in the plot, highlighting a slight but systematic tendency toward elongation. Similar reduction in aspect ratio in 1D compression has been observed for calcareous

678 sands by Wei et al. (2022).

679

680 A similar trend is observed for the 32.4% Diest Glauconite and 7.8% Vlierzele Glauconite samples (Fig. 23 (b)
681 and Fig. 23 (c)). In both cases, the aspect ratio distributions are unimodal, with peaks near α=0.6-0.72, and the
682 most significant change occurs between the initial state and the first breakage stage (B_r=0.262 for 32.4% Diest
683 and B_r=0.423 for 7.8% Vlierzele). This shift is primarily associated with a decrease in more equant particles and
684 a corresponding increase in elongated and sub-elliptical particles ($\alpha \approx$0.3-0.65). At higher breakage levels
685 (B_r=0.654-0.955 for 32.4% Diest and B_r=0.707-0.993 for 7.8% Vlierzele), the distributions nearly overlap,
686 suggesting that particle shapes stabilize after the first fragmentation stage. The mean aspect ratio decreases
687 modestly from α_0=0.683 to α_L=0.634 for the 32.4% Diest Glauconite and from α_0=0.665 to α_L=0.625 for the 7.8%
688 Vlierzele Glauconite, confirming a gradual but limited elongation trend and the overall tendency of glauconitic
689 grains to preserve their original geometry.

690

691 In contrast, the 100% silica sand sample (Fig. 23 (d)) exhibits the most distinct evolution of shape among the
692 tested materials. The distribution, initially peaked at α=0.725, shifts noticeably after the first breakage level
693 (B_r=0.167), where the frequency of elongated and part of sub-elliptical particles (α<0.6) increases and that of
694 equant particles (α>0.675) decreases. Subsequent breakage (B_r=0.609-0.996) introduces only minor variations.
695 The mean aspect ratio decreases from α_0=0.686 to α_L=0.623, indicating a more pronounced elongation tendency
696 associated with the brittle fracture of quartz grains.

697

698 Overall, all materials exhibit unimodal aspect ratio distributions, with peaks consistently cantered around α=0.6-
699 0.72. The largest change in relative frequency occurs between the initial condition and the first breakage level,

indicating that particle elongation primarily develops during the early stage of fragmentation. Thereafter, the distributions remain largely stable, suggesting limited additional morphological modification with further breakage. Although glauconite is more susceptible to crushing, glauconitic grains exhibit only minor elongation, whereas silica sand shows a more pronounced elongation trend, reflecting the brittle fracture characteristics of quartz grains.

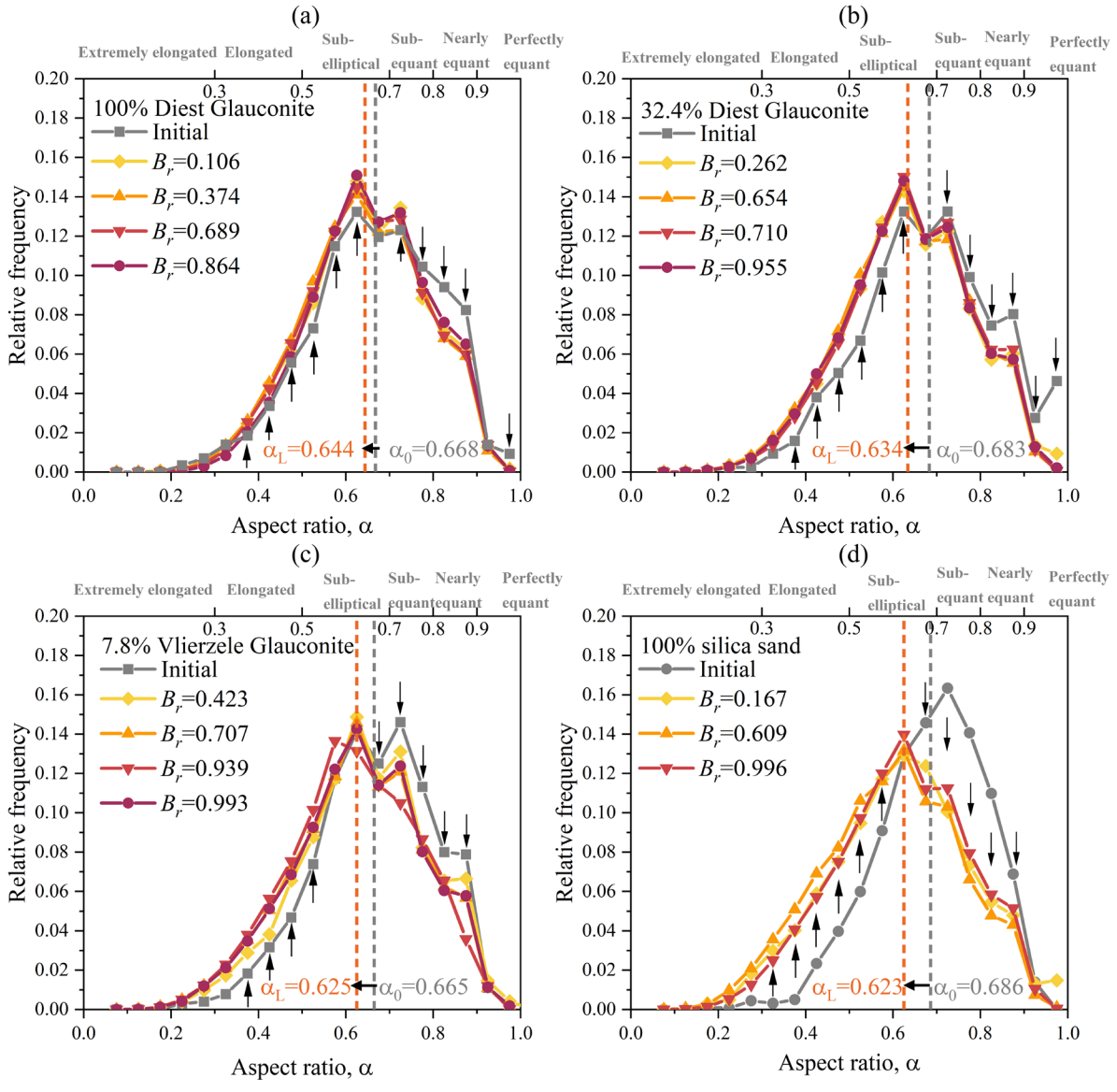

Fig. 22. Relative frequency distributions of particle aspect ratio for samples with varying glauconite content: (a) 100% Diest Glauconite, (b) 32.4% Diest Glauconite, (c) 7.8% Vlierzele Glauconite, and (d) 100% silica sand. The

709 classification labels at the top of each subplot indicate the qualitative categories associated with the corresponding
710 parameter ranges
711
712 The evolution of sphericity, roundness, and circularity for the 100% Diest Glauconite and 100% silica sand
713 samples at different levels of relative breakage is presented in Fig. 24. For both materials, the distributions of all
714 three shape descriptors are unimodal, indicating consistent overall shape populations during breakage. For Diest
715 Glauconite (Fig. 24 (a)), the sphericity values across different relative breakage levels are mostly concentrated
716 between 0.85-0.98, i.e., 90% of sphericity values, corresponding to sub-spherical to nearly spherical particles.
717 With increasing relative breakage (B_r=0.106-0.864), only minor shifts occur in the frequency curves, indicating
718 that glauconite particles retain their overall compact geometry. Similarly, the distributions of circularity of
719 glauconite exhibit negligible change, with modal value remaining around 0.8-0.9. However, the roundness
720 distributions exhibit a noticeable increase in frequency within the 0.5-0.6 range and a decrease in 0.625-0.8,
721 indicating particle edges become slightly more irregular due to abrasion and crushing (as illustrated in Fig. 16).
722 These results confirm that although glauconite particles undergo breakage, their shapes become slightly more
723 elongated and their edges slightly sharper, their overall outlines and smoothness are largely preserved. This
724 observation is consistent with the limited reduction in mean sphericity and circularity shown in Fig. 22.
725
726 In contrast, the silica sand (Fig. 24 (b), (d) and (f)) exhibits more pronounced changes in all three descriptors as
727 breakage progresses (B_r= 0.167-0.996). The sphericity distributions flatten near their modal values (0.9-0.925)
728 and show a minor increase in relative frequency at sphericity<0.85, indicating a reduction in the population of
729 near-spherical particles and a gradual increase in elongation due to the formation of elongated and angular
730 fragments. The roundness distributions shift slightly toward lower values, with an increase in the relative

731 frequency of shaper-edged particles (roundness < 0.575). The circularity distributions follow a similar trend to
732 sphericity, with reduced frequency at modal values (≈0.775-0.875) and increased frequency at circularity<0.675,
733 reflecting more irregular particle outlines. Together, these results indicate that the brittle fracture of quartz grains
734 produces more distinct angularity and a greater loss of compactness compared with the more plastic glauconitic
735 particles.
736
737 In summary, the relative frequency data in Fig. 23 and Fig. 24 corroborate the mean-value trends presented in Fig.
738 22. The largest shape modification occurs during the initial breakage stages, after which the distributions stabilize,
739 implying that most shape evolution is controlled by the onset of crushing. While glauconitic grains show minor
740 elongation and retain near-equant geometries, silica sand particles become progressively more elongated and
741 angular, demonstrating a stronger mechanical response to crushing.

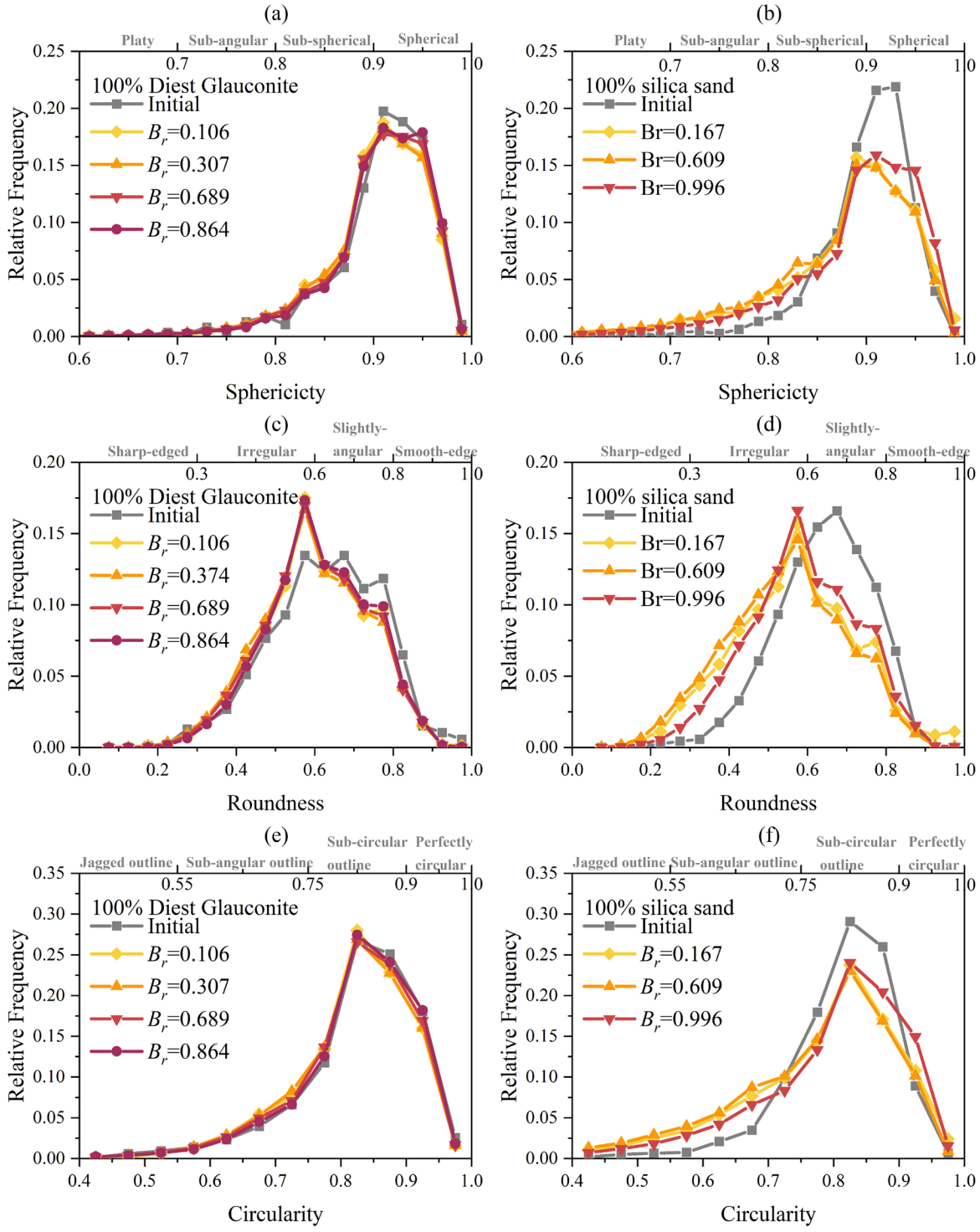

Fig. 23. Relative frequency distributions of (a-b) sphericity, (c-d) roundness, and (e-f) circularity for 100% Diest Glauconite and 100% silica sand at different levels of relative breakage. The classification labels at the top of each subplot indicate the qualitative categories associated with the corresponding parameter ranges

4. Discussion

A programme of 1D compression tests have been performed on pure glauconite sands, glauconite-silica sand mixtures and pure silica sand to systematically characterise their mechanical response, crushing behaviour, and particle-scale evolution. The arrested loading-unloading approach, combined with detailed particle size and shape analyses, provides high confidence in the repeatability of the mechanical response and enables direct observation of particle size/shape evolution, thereby supporting the development of quantitative relationships that describe the evolution of particle size and shape.

The stress-strain behaviour of pure glauconite sands, glauconite-silica sand mixtures and pure silica sand has been compared systematically for the first time under 1D compression. The results reveal a clear dependence on glauconite content, with increasing glauconite content leading to reduced stiffness, lower stress, lower yielding stress and diminished work input at yielding. Quantitative analysis further shows that both yielding stress and work input at yielding decreases exponentially with increasing glauconite content, yielding strong power-law relationships (R^2> 0.92) that confirm the dominant influence of glauconite content on mechanical strength and energy absorption capacity (Fig. 10).

The incremental loading tests reveal time-dependent deformation and clay-like behaviour in saturated glauconite, while comparison across loading patterns and saturation conditions shows that water markedly reduces stiffness, yield stress, and energy absorption capacity, which is an effect far more pronounced in glauconite than in silica sand. Quantitative comparisons further demonstrate that water saturation weakens glauconite by up to 88.2% at 30% strain, whereas silica sand exhibits only a 35.3% reduction, confirming the substantially higher water sensitivity and structural vulnerability of glauconite under 1D compression. This strong water sensitivity aligns

769 with findings that hydration promotes glauconite disaggregation and the release of clay minerals, weakening the
770 granular skeleton and reducing particle strength (Westgate et al., 2023).
771
772 The PSD results clearly show that all tested materials progressively evolve toward finer grading with increasing
773 axial strain, with the relative breakage index B_r increasing approximately linearly with strain. This behaviour is
774 consistent with observations on quartz and carbonate sands subjected to high compressive stresses, with PSDs
775 converging toward a stable fractal form (McDowell et al., 1996; Coop et al., 2004; Russell, 2011; Xiao et al., 2016;
776 Huang et al., 2017). Such crushable granular materials typically approach ultimate fractal dimensions in the range
777 of approximately 2.3-2.95 under large strains (Perfect, 1997; McDowell and Bolton, 1998; Coop et al., 2004;
778 Russell, 2010; Huang et al., 2017; Li et al., 2022). The increasing fractal dimension D_s observed here, along with
779 its asymptotic tendency toward material-dependent ultimate values D_{su}, aligns closely with this established
780 "fractal crushing" paradigm. What distinguishes the present work is the explicit quantitative links between B_r, D_s,
781 and specific work W. Although previous studies have linked B_r to either D_s or input energy (Huang et al., 2014,
782 2017; Xiao et al., 2019), they have seldom demonstrated mutually consistent relationships. The B_r and D_s
783 relationship established in this study provide a compact descriptor of PSD evolution that links a widely used
784 engineering index (B_r) with a physically grounded grading descriptor (D_s). When combined with the observed
785 D_s-W and B_r-W trends, these results form a unified experimental framework that captures how grading, breakage,
786 and energy dissipation co-evolve during crushing. This framework is applicable to both glauconitic materials and
787 conventional silica sands, and it deepens the understanding of how particle breakage progresses toward a ultimate
788 state.
789
790 The reduction in aspect ratio, roundness, sphericity and circularity with increasing breakage are broadly consistent

791 with earlier imaging studies on quartz, carbonate, and calcareous sands, which show that fragmentation tends to
792 generate particles that are more elongated and angular particles (Buscarnera and Einav, 2021; Wei et al., 2022;
793 Yao et al., 2023). Buscarnera and Einav (2021) proposed a theoretical relationship linking the evolution of mean
794 aspect ratio α to relative breakage B_r, and the present results demonstrate that this mathematical work can be
795 extended to captures the evolution of additional shape descriptors, namely roundness, sphericity, and circularity
796 (Fig. 22). Beyond this general trend, the shape evolution extracted from large-scale statistical datasets (several
797 thousand to tens of thousands of particles) further reveals clear material-specific breakage mechanisms. In
798 particular, pure silica sand develops slightly stronger elongation and irregularity than pure glauconite at equivalent
799 or comparable strain, despite its higher macroscopic strength. This finding highlights that mineralogy governs not
800 only the rate of PSD evolution but also the pathways of shape transformation, a feature rarely quantified in earlier
801 breakage studies.
802
803 By integrating particle size evolution, fractal dimension, and particle shape evolution, this study establishes a
804 unified experimental-analytical framework (Fig. 25) that links particle-scale breakage to macroscopic strength,
805 compressibility, and work input. This framework not only advances the fundamental understanding of glauconite
806 sands, whose breakage behaviour remains insufficiently documented in engineering practice, but also provides an
807 experimental basis for developing analytical tools that must incorporate grading evolution, particle morphology,
808 and mineral-dependent breakage mechanisms. Future research may extend this framework to more complex
809 loading paths, including generalized triaxial and cyclic compression conditions. High-resolution 3D imaging
810 techniques such as X-ray CT with digital volume correlation, combined with automated particle segmentation,
811 could further elucidate how particle breakage and intra-particle structure control the bulk mechanical response. In
812 parallel, the mechanisms through which water transforms glauconite into a clay-like material should be explored

using advanced mineralogical and micro-mechanical methods, including environmental SEM, in-situ nano-indentation, and micro-CT under controlled saturation.

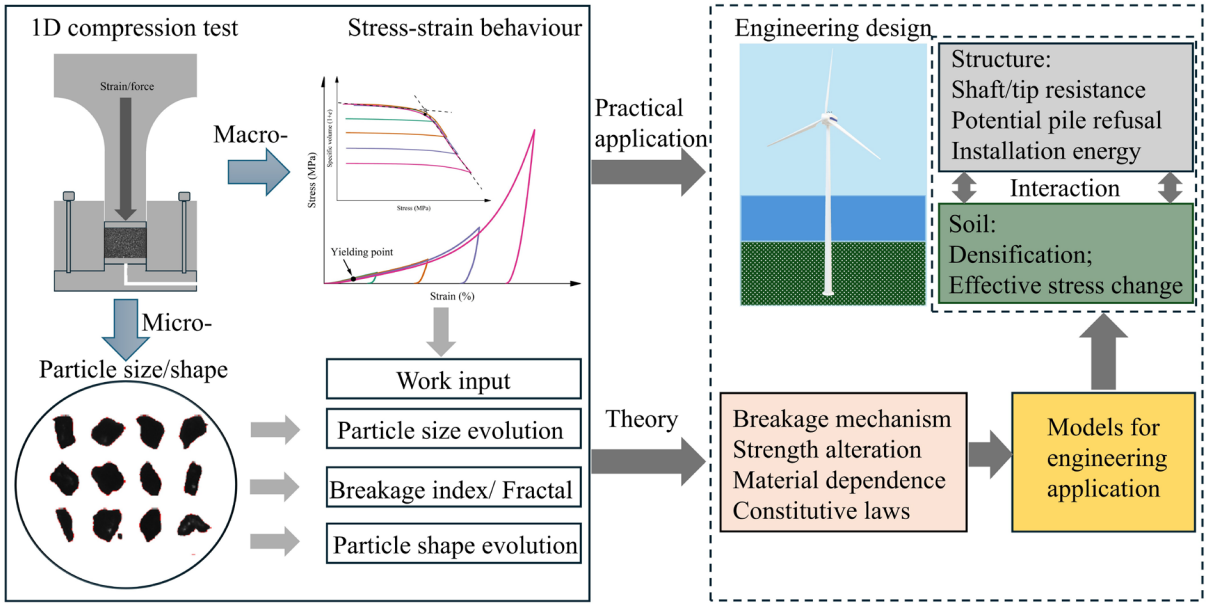

Fig. 24. Experimental and analytical framework linking 1D compression behaviour with particle-scale evolution (size, breakage, and shape) and its potential translation into geotechnical engineering applications.

5. Conclusion

CRediT authorship contribution statement

Shijin Li: Conceptualization, Methodology, Investigation, Formal analysis, Data curation, Validation, Software, Writing-original draft, Visualization; **Hannes Claes**: Resources, Investigation, Writing-review & editing; **Hadrien Rattez**: Conceptualization, Supervision, Project administration, Resources, Funding acquisition,

827 Writing-review & editing.

828 **Declaration of Competing interest**

829 The authors declare that they have no competing financial interests or personal relationships that could have
830 appeared to influence the work reported in this paper.

831

832 **Acknowledgments and funding**

833 The authors gratefully acknowledge the financial support provided by the Belgian Energy Transition Fund (ETF)
834 through the SAGE-SAND project *"Soil Aging Around Offshore Wind Turbine Foundations - From Operational*
835 *Response to Decommissioning"* (Grant No. 3E220974), as well as the support from the National Natural Science
836 Foundation of China (Grant No. 52308370).

837

838 **Data availability statement**

839 All experimental data supporting the results of this study are available from the first author, Shijin Li, upon
840 reasonable request.

841 **Conflict of interest**

842 The authors declare that they have no conflict of interest.

843

844 **Notation list**

845 **REFERECES**

846 Altuhafi, F., O'Sullivan, C., Cavarretta, I., 2013. Analysis of an Image-Based Method to Quantify the Size and
847 Shape of Sand Particles. J. Geotech. Geoenviron. Eng. 139, 1290–1307.
848 https://doi.org/10.1061/(ASCE)GT.1943-5606.0000855

849 ASTM D2435, 2020. Test Methods for One-Dimensional Consolidation Properties of Soils Using Incremental
850 Loading. https://doi.org/10.1520/D2435

851 Baldermann, A., Banerjee, S., Czuppon, G., Dietzel, M., Farkaš, J., Löhr, S., Moser, U., Scheiblhofer, E., Wright,
852 N.M., Zack, T., 2022. Impact of green clay authigenesis on element sequestration in marine settings. Nat
853 Commun 13, 1527. https://doi.org/10.1038/s41467-022-29223-6

854 Bellotti, R., Fretti, C., Ghionna, V.N., Pedroni, S., 1991. Compressibility and crushability of sands at high stresses,
855 in: Proceedings of the First International Symposium on Calibration Chamber Testing. pp. 79–90.

856 Born, M., Wolf, E., 2013. Principles of Optics: Electromagnetic Theory of Propagation, Interference and
857 Diffraction of Light. Elsevier.

858 Buscarnera, G., Einav, I., 2021. The mechanics of brittle granular materials with coevolving grain size and shape.
859 Proc. R. Soc. A. 477, rspa.2020.1005, 20201005. https://doi.org/10.1098/rspa.2020.1005

860 Cavarretta, I., Coop, M., O'Sullivan, C., 2010. The influence of particle characteristics on the behaviour of coarse
861 grained soils. Géotechnique 60, 413–423. https://doi.org/10.1680/geot.2010.60.6.413

862 Ciantia, M.O., O'Sullivan, C., 2020. Calculating the State Parameter in Crushable Sands. Int. J. Geomech. 20,
863 04020095. https://doi.org/10.1061/(ASCE)GM.1943-5622.0001707

864 Coop, M.R., Sorensen, K.K., Freitas, T.B., Georgoutsos, G., 2004. Particle breakage during shearing of a

carbonate sand. Géotechnique 54, 157–163. https://doi.org/10.1680/geot.2004.54.3.157

De Nijs, R.E.P., Kaalberg, F.J., Osselaer, G., Couck, J. van, Van Royen, K., 2015. Full-scale field test (sheet) pile drivability in Antwerp (Belgium).

Einav, I., 2007a. Breakage mechanics—Part II: Modelling granular materials. Journal of the Mechanics and Physics of Solids 55, 1298–1320. https://doi.org/10.1016/j.jmps.2006.11.004

Einav, I., 2007b. Breakage mechanics—Part I: Theory. Journal of the Mechanics and Physics of Solids 55, 1274–1297. https://doi.org/10.1016/j.jmps.2006.11.003

Emidio, Verástegui Flores R.D., Van Impe W.F., 2009. Crushability of Granular Materials at High Stress Levels, in: Proceedings of the 17th International Conference on Soil Mechanics and Geotechnical Engineering. IOS Press. https://doi.org/10.3233/978-1-60750-031-5-127

Eshel, G., Levy, G.J., Mingelgrin, U., Singer, M.J., 2004. Critical Evaluation of the Use of Laser Diffraction for Particle-Size Distribution Analysis. Soil Science Soc of Amer J 68, 736–743. https://doi.org/10.2136/sssaj2004.7360

Grubbs, J., Tsaknopoulos, K., Massar, C., Young, B., O'Connell, A., Walde, C., Birt, A., Siopis, M., Cote, D., 2021. Comparison of laser diffraction and image analysis techniques for particle size-shape characterization in additive manufacturing applications. Powder Technology 391, 20–33. https://doi.org/10.1016/j.powtec.2021.06.003

Ham, T.-G., Nakata, Y., Orense, R., Hyodo, M., 2010. Influence of Water on the Compression Behavior of Decomposed Granite Soil. J. Geotech. Geoenviron. Eng. 136, 697–705. https://doi.org/10.1061/(ASCE)GT.1943-5606.0000274

Hardin, B.O., 1985. Crushing of Soil Particles. J. Geotech. Engrg. 111, 1177–1192. https://doi.org/10.1061/(ASCE)0733-9410(1985)111:10(1177)

887 Hossain, Z., Fabricius, I.L., Christensen, H.F., 2009. Elastic and nonelastic deformation of greensand. The Leading
888 Edge 28, 86–88.
889 Huang, J., Xu, S., Hu, S., 2014. Influence of particle breakage on the dynamic compression responses of brittle
890 granular materials. Mechanics of Materials 68, 15–28. https://doi.org/10.1016/j.mechmat.2013.08.002
891 Huang, J.Y., Hu, S.S., Xu, S.L., Luo, S.N., 2017. Fractal crushing of granular materials under confined
892 compression at different strain rates. International Journal of Impact Engineering 106, 259–265.
893 https://doi.org/10.1016/j.ijimpeng.2017.04.021
894 Jiang, H., Li, Y., Huang, Q., Xue, D., Buscarnera, G., 2026. Numerical identification of size-shape-strength
895 attractors in sheared breakable granular materials. Computers and Geotechnics 190, 107709.
896 https://doi.org/10.1016/j.compgeo.2025.107709
897 Konstantinou, M., Piedrabuena, A.R., Hellebrekers, N., Mirko Mento, Ahmed Elkadi, Ken Gavin, 2025.
898 Geotechnical Properties of a Glauconite Sand from Belgium. ISSMGE.
899 https://doi.org/10.53243/ISFOG2025-65
900 Lei, J., Arroyo, M., Ciantia, M., Zhang, N., 2024. A fracture-based discrete model for simulating creep in quartz
901 sands. Géotechnique 1–43. https://doi.org/10.1680/jgeot.23.00068
902 Li, X., Liu, J., Li, J., 2022. Fractal dimension, particle shape, and particle breakage analysis for calcareous sand.
903 Bull Eng Geol Environ 81, 106. https://doi.org/10.1007/s10064-022-02585-3
904 Manso, J., Marcelino, J., Caldeira, L., 2018. Crushing and oedometer compression of rockfill using DEM.
905 Computers and Geotechnics 101, 11–22. https://doi.org/10.1016/j.compgeo.2018.04.009
906 McDowell, G.R., Bolton, M.D., 1998. On the micromechanics of crushable aggregates. Géotechnique 48, 667–
907 679. https://doi.org/10.1680/geot.1998.48.5.667
908 McDowell, G.R., Bolton, M.D., Robertson, D., 1996. The fractal crushing of granular materials. J. Mech. Phys.

909 Solids 44, 2079–2101. https://doi.org/10.1016/S0022-5096(96)00058-0
910 McDowell, G.R., De Bono, J.P., 2013. On the micro mechanics of one-dimensional normal compression.
911 Géotechnique 63, 895–908. https://doi.org/10.1680/geot.12.P.041
912 McDowell, G.R., Humphreys, A., 2002. Yielding of granular materials. Granul. Matter. 4, 1–8.
913 https://doi.org/10.1007/s10035-001-0100-4
914 Mentiki, C., Davis, J., Semertzidou, K., Abbireddy, C.O.R., Hight, D.W., Williams, D., Black, M., 2015. The
915 Geology and Geotechnical Properties of the Thanet Sand Formation. Part of Crossrail Project from
916 Department for Transport, London.
917 Miura, N., Toyotoshi, Y., 1975. Effect of water on the behavior of a quartz-rich sand under high stresses. Soils
918 Found. 15, 23–34.
919 Muir Wood, D., 2007. The magic of sands. Can. Geotech. J. 44, 1329–1350. https://doi.org/10.1139/T07-060
920 Nakata, Y., Hyodo, M., Hyde, A.F.L., Kato, Y., Murata, H., 2001. Microscopic Particle Crushing of Sand Subjected
921 to High Pressure One-Dimensional Compression. Soils and Foundations 41, 69–82.
922 https://doi.org/10.3208/sandf.41.69
923 Perfect, E., 1997. Fractal models for the fragmentation of rocks and soils: a review. Engineering Geology 48, 185–
924 198. https://doi.org/10.1016/S0013-7952(97)00040-9
925 Perikleous, G., Meissl, S., Diaz, A.T., Stergiou, T., Ridgway-Hill, A., 2023. Monopile installation in glauconitic
926 sands, in: 9th International SUT Offshore Site Investigation Geotechnics Conference Proceedings
927 “Innovative Geotechnologies for Energy Transition.” Presented at the Innovative Geotechnologies for
928 Energy Transition, Society of Underwater Technology, pp. 132–138. https://doi.org/10.3723/JBWL5180
929 Russell, A.R., 2011. A compression line for soils with evolving particle and pore size distributions due to particle
930 crushing. Géotechnique Letters 1, 5–9. https://doi.org/10.1680/geolett.10.00003

931 Russell, A.R., 2010. Water retention characteristics of soils with double porosity. Eur. J. Soil Sci. 61, 412–424.
932 Russell, A.R., Muir Wood, D., 2009. Point load tests and strength measurements for brittle spheres. International
933 Journal of Rock Mechanics and Mining Sciences 46, 272–280.
934 https://doi.org/10.1016/j.ijrmms.2008.04.004
935 Storti, F., Billi, A., Salvini, F., 2003. Particle size distributions in natural carbonate fault rocks: insights for non-
936 self-similar cataclasis. Earth and Planetary Science Letters 206, 173–186. https://doi.org/10.1016/S0012-
937 821X(02)01077-4
938 Suescun-Florez, E., Iskander, M., Bless, S., 2020. Evolution of particle damage of sand during axial compression
939 via arrested tests. Acta Geotech. 15, 95–112. https://doi.org/10.1007/s11440-019-00892-w
940 Tedrow, J.C.F., 2002. Greensand and greensand soils of New Jersey: a review. Rutgers Cooperative Extension, NJ
941 Agricultural Experiment Station, Rutgers, the State University of New Jersey.
942 Ventouras, K., Coop, M.R., 2009. On the behaviour of Thanet Sand: an example of an uncemented natural sand.
943 Géotechnique 59, 727–738. https://doi.org/10.1680/geot.7.00061
944 Wang, X., Yang, D., Liu, C., Li, M., 2026. Experimental and theoretical quantification of in-situ crushing
945 characteristics of irregularly-shaped particles under multi-axis pressure with X-ray micro-computed
946 tomography (μCT) and discrete element method (DEM). Powder Technology 469, 121733.
947 https://doi.org/10.1016/j.powtec.2025.121733
948 Wei, H., Liu, H., Zhao, T., Zhang, S., Ma, L., Yin, M., Meng, Q., 2022. Particle breakage and morphology changes
949 of calcareous sands under one-dimensional compression loading. Mar Geophys Res 43, 45.
950 https://doi.org/10.1007/s11001-022-09507-8
951 Westgate, Z., McMullin, C., DeGroot, D., 2022. Glauconite Sand Challenges for US Offshore Wind Development,
952 in: ASME 2022 4th International Offshore Wind Technical Conference. Presented at the ASME 2022 4th

International Offshore Wind Technical Conference, American Society of Mechanical Engineers, Boston, Massachusetts, USA, p. V001T02A002. https://doi.org/10.1115/IOWTC2022-98666

Westgate, Z., Rahim, A., Senanayake, A., Pisanò, F., Maldonado, C., Ridgway-Hill, A., Perikleous, Y., De Sordi, J., Roux, A., Andrews, E., Ghasemi, P., 2024. The Piling in Glauconitic Sands (PIGS) JIP: Reducing Geotechnical Uncertainty for U.S. Offshore Wind Development, in: Day 3 Wed, May 08, 2024. Presented at the Offshore Technology Conference, OTC, Houston, Texas, USA, p. D031S001R007. https://doi.org/10.4043/35483-MS

Westgate, Z.J., DeGroot, D.J., McMullin, C., Zou, Y., Guo, D., Van Haren, S., Beemer, R.D., Zeppilli, D., Miller, K.G., Browning, J.V., 2023. Effect of degradation on geotechnical behavior of glauconite sands from the U.S. Mid-Atlantic Coastal Plain. Ocean Engineering 283, 115081. https://doi.org/10.1016/j.oceaneng.2023.115081

Wils, L., Haegeman, W., 2014. One-dimensional compression of a crushable sand in dry and wet conditions, in: Soga, K., Kumar, K., Biscontin, G., Kuo, M. (Eds.), Geomechanics from Micro to Macro. CRC Press, pp. 1403–1408. https://doi.org/10.1201/b17395-254

Wu, Y., Yamamoto, H., Cui, J., Cheng, H., 2020. Influence of Load Mode on Particle Crushing Characteristics of Silica Sand at High Stresses. Int. J. Geomech. 20, 04019194. https://doi.org/10.1061/(ASCE)GM.1943-5622.0001600

Xiao, Y., Liu, H., Chen, Q., Ma, Q., Xiang, Y., Zheng, Y., 2017. Particle breakage and deformation of carbonate sands with wide range of densities during compression loading process. Acta Geotech. 12, 1177–1184. https://doi.org/10.1007/s11440-017-0580-y

Xiao, Y., Liu, H., Xiao, P., Xiang, J., 2016. Fractal crushing of carbonate sands under impact loading. Géotechnique Letters 6, 199–204. https://doi.org/10.1680/jgele.16.00056

975 Xiao, Y., Yuan, Z., Chu, J., Liu, H., Huang, J., Luo, S.N., Wang, S., Lin, J., 2019. Particle breakage and energy
976 dissipation of carbonate sands under quasi-static and dynamic compression. Acta Geotech. 14, 1741–
977 1755. https://doi.org/10.1007/s11440-019-00790-1
978 Yao, T., Xing, X., Li, W., 2023. Evolution of particle morphology of quartz sand during one-dimensional
979 compression. Powder Technology 429, 118921. https://doi.org/10.1016/j.powtec.2023.118921
980 Yu, F., 2017. Characteristics of particle breakage of sand in triaxial shear. Powder Technology 320, 656–667.
981 https://doi.org/10.1016/j.powtec.2017.08.001
982 Zhang, Y.D., Buscarnera, G., Einav, I., 2016. Grain size dependence of yielding in granular soils interpreted using
983 fracture mechanics, breakage mechanics and Weibull statistics. Géotechnique 66, 149–160.
984 https://doi.org/10.1680/jgeot.15.P.119
985 Zhao, B., Wang, J., Andò, E., Viggiani, G., Coop, M.R., 2020. Investigation of particle breakage under one-
986 dimensional compression of sand using X-ray microtomography. Can. Geotech. J. 57, 754–762.
987 https://doi.org/10.1139/cgj-2018-0548
988 Zou, Y., DeGroot, D.J., Westgate, Z.J., 2025. Direct and Interface Shear Behavior of an Authigenic Glauconite
989 Sand from the Coastal Plain of New Jersey. J. Geotech. Geoenviron. Eng. 151, 04025065.
990 https://doi.org/10.1061/JGGEFK.GTENG-13275
991

992

993